Adaptable Swarm Sensing in Coastal Waters: Design and Performance of the μFloat System

Trevor W. Harrison
Applied Physics Laboratory
University of Washington
Seattle, WA 98195
twharr@uw.edu

Corey Crisp
Mechanical Engineering
University of Washington
Seattle, WA 98195
cappy85@uw.edu

Jessica Noe
Applied Physics Laboratory
University of Washington
Seattle, WA 98195
noej@uw.edu

James B. Joslin
Applied Physics Laboratory
University of Washington
Seattle, WA 98195
jbjoslin@uw.edu

Cassie Riel
Applied Physics Laboratory
University of Washington
Seattle, WA 98195
criel@uw.edu

Matthew Dunbabin
School of Electrical Engineering & Robotics
Queensland University of Technology
Brisbane, Australia
m.dunbabin@qut.edu.au

Jeffrey Neasham
School of Engineering
Newcastle University
Newcastle upon Tyne, UK
jeff.neasham@newcastle.ac.uk

Timothy R Mundon
Oscilla Power, Inc.
Seattle, WA 98199
mundon@oscillapower.com

Brian Polagye
Mechanical Engineering
University of Washington
Seattle, WA 98195
bpolagye@uw.edu

Abstract

Buoyancy-controlled underwater floats have produced a wealth of *in situ* observational data from the open ocean. When deployed in large numbers, or 'swarms', floats offer a unique capacity to concurrently map 3D fields of critical environmental variables, such as currents, temperatures, and dissolved oxygen. This sensing paradigm is equally relevant in coastal waters, yet remains underutilized due to economic and technical limitations of existing platforms. To address this gap, we developed a swarm of 25 μFloats that can actuate vertically in the water column by controlling their buoyancy, but are otherwise Lagrangian. Underwater positioning is achieved by acoustic localization using low-bandwidth communication with GPS-equipped surface buoys. The μFloat

features a high-volume buoyancy engine that provides a 9% density change, enabling automatic ballasting and vertical control from fresh to salt water ($\sim$ 3% density change) with reserve capacity for external sensors. In this paper, we present design specifications and field benchmarks for buoyancy control and acoustic localization accuracy. Results demonstrate depth-holding accuracy within $\pm$0.2 m of target depth in quiescent flow and $\pm$0.5 m in energetic flows. Underwater localization is accurate to within $\pm$5 m during periods with sufficient connectivity, with degradation in performance resulting from adverse sound speed gradients and unfavorable surface buoy array geometry. Support for auxiliary sensors (<10% float volume) without additional control tuning is also demonstrated. Overall performance is discussed in the context of potential use cases and demonstrated in a first-ever swarm-based three-dimensional survey of tidal currents.

1 Introduction

Oceanographic floats, most notably the Argo program, have dramatically improved our understanding of ocean circulation and expanded the spatial and temporal distribution of worldwide salinity and temperature measurements (Riser et al., 2016; Jayne et al., 2017; Wong et al., 2020; Gould, 2005; Rossby, 2007). When considering the *in situ* sensing needs to support monitoring, simulation, and management of coastal waterways (Arkema et al., 2015; Wilkin et al., 2017; Liu et al., 2015; Fringer et al., 2019), multitudes of floats (i.e., 'swarms') are a conceptually attractive approach. However, floats designed for the global ocean are not well-suited to coastal environments. Oceanographic floats include pressure housings and hydraulic buoyancy control systems for 2000 m dives and can tolerate relatively low accuracy depth control of $O(10)$ m. Coastal waters extend from estuarine systems out to the continental shelf and have a maximum depth of roughly 200 m (Bowden, 1983). These shallower waters necessitate higher accuracy $O(1)$ m depth control, but lower hydrostatic pressures permit simpler (and less expensive) mechanical buoyancy engines (D'Asaro, 2003; Jaffe et al., 2017). Similarly, oceanographic floats are deployed for long durations (weeks to years), often without intention of recovery. Thus, data communication is accomplished via satellite. In coastal environments, smaller horizontal domains O(1-10) km permit inexpensive hardware recovery and operations within the range of cellular and radio communication, eliminating the reliance on satellite communication. Lastly, coastal environments can exhibit strong density gradients where fresh river water enters coastal seas or be well-mixed in regions with strong tidal currents. A coastal float must accommodate both conditions.

A small number of floats suitable for coastal environments do exist. The sole commercial example is MRV Systems' ALAMO float. While designed for open-ocean research (e.g., rapid deployment in front of hurricanes and under-ice profiling in the Arctic (Jayne and Bogue, 2017)), it is sufficiently small ($\sim$ 1 m tall, 9 kg) to permit shallow water deployments and its buoyancy engine can accommodate the density gradients present in coastal waters. The

remaining examples are custom platforms developed by individual research groups. D'Asaro et al. developed the MLF float (D'Asaro et al., 1996; D'Asaro, 2003) for 3D Lagrangian flow-following to study convection, vertical velocity, vorticity, and turbulent mixing in the upper-ocean (< 300 m) mixed layer, as well as in large scale tidal channels (Alford et al., 2005; Steffen and D'Asaro, 2002; D'Asaro and Dairiki, 1997; D'Asaro and Lien, 2000; Lien et al., 1998; D'Asaro et al., 2002; D'Asaro, 2014; Shcherbina et al., 2018). The MLF can also measure internal waves, surface waves, and upwelling (Lien et al., 2002; D'Asaro, 2015, 2004). Roman et al. developed a coastal float equipped with bottom-tracking and a downward-looking camera for visual benthic explorations (Schwithal and Roman, 2009; McGilvray and Roman, 2010; Roman et al., 2011), and later combined thruster and buoyancy-control for improved vertical actuation accuracy and efficiency (Snyder et al., 2018). While the previously mentioned profiling, Lagrangian, and bottom-tracking floats are roughly 1 m scale, Jaffe et al. designed the miniature Autonomous Underwater Explorer (M-AUE) with a form factor of roughly 0.2 m to better emulate passive and vertically-migrating larvae, as well as improve measurements of submesoscale ocean dynamics (Jaffe et al., 2017). With a swarm (16 floats), they demonstrated plankton patch formation in internal waves on the California continental shelf. More recently, higher capacity coastal floats have been developed for observing biogeochemical processes (Schulze Chretien and Speer, 2018) (Gene Massion, pers. comm.), though their expense and size hinder swarm deployments.

Inspired by the success of these groups, the objective of this work was to develop an inexpensive coastal float swarm (Fig. 1). The new float, dubbed the μFloat ("microFloat"), fills the gap in operational space between the capabilities and form factors of existing floats and reduces unit costs by leveraging recent advancements in oceanographic and electronic technology. In Section 2, we describe the overall design of the μFloat, with the buoyancy engine implementation and evaluation described in Section 3. In Section 4, we describe the underwater localization system and undertake field testing in quiescent water (Lake Washington, WA). Finally, in Section 5, we demonstrate the full swarm system in an energetic tidal channel (Agate Pass, WA). Comparison between quiescent benchmarks and dynamic performance are presented in Section 5. We finish by discussing implications for future sampling objectives in Section 6.

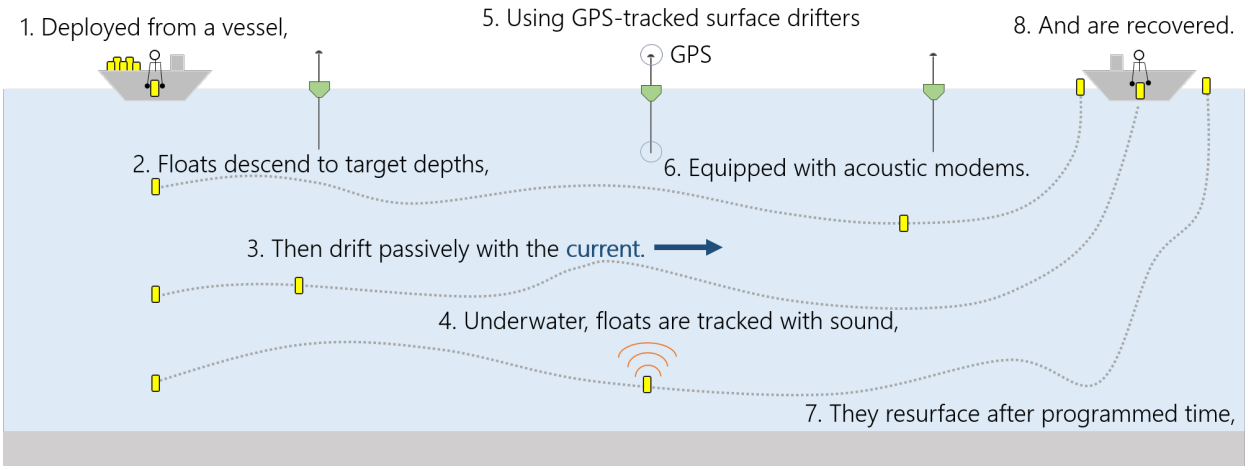

Figure 1: μFloat operational concept from deployment, dive to target depth, transport with water currents, and resurfacing for recovery.

2 μFloat Design

2.1 Design

The μFloats were designed for short-duration sampling ($\leq$ 1 day) of quickly evolving phenomena ($O(10)$ minutes; e.g., eddies) in coastal waters. Regions of interest have small horizontal ranges ($O(1)$ km), but exhibit strong spatial gradients that necessitate high spatial sample resolution ($O(10)$ m). Operational depths may range from 10-100 m and flow speeds may exceed 1 m/s. Water density may vary by as much as 3% (fresh to salt water) or be well-mixed. Given this environment and the intended 'swarm' sampling strategy, the μFloats were designed with the following requirements:

1. Depth-holding accuracy within 1 m to provide vertical coverage throughout a 100 m water column.

2. Movement to target depth is achieved quickly ($<$ 5 minutes).

3. Float horizontal position is resolved to within 10 m at minimum 1 km range.

4. Horizontal positions are updated at least once per 10 seconds.

5. Rapid recovery and redeployment are possible, enabling repeat surveys in the region of interest.

6. Individual units are easily handled by a single person without special equipment to minimize operational costs.

7. Unit costs are minimized.

2.2 Implementation

2.2.1 μFloat Architecture

The μFloat (Fig. 2) was designed to be as small as possible while respecting constraints for low-cost electronics, future sensor suite expansion, and buoyancy engine capacity. Costs were minimized through the use of hobbyist and commercial-off-the-shelf parts wherever possible and all custom components were designed for inexpensive production and assembly. The main housing is a 13 cm (4") diameter, 40 cm long acrylic tube with double O-ring piston seals (Blue Robotics) and custom end caps. It has a rated depth of 100 m.

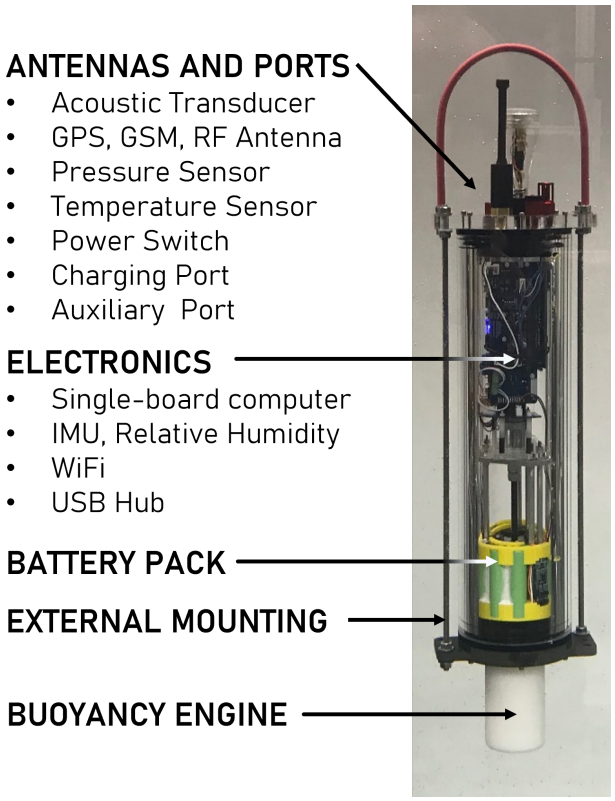

Figure 2: μFloat with annotated core subsystems.

The μFloat can position itself vertically in the water column by manipulating its density relative to the surrounding water through the use of a "buoyancy engine". The buoyancy engine is comprised of a solid acetal (Delrin) piston that extends through a T-ring seal in the bottom end cap. Actively controlling the piston extension changes the total displaced volume of the float while mass remains constant, thus changing the float density. The piston is driven by a lead screw connected to a brushed DC motor with planetary gearbox (ServoCity) and motor controller (Pololu). Piston position is inferred by a quadrature encoder attached to the motor shaft and limit switches are mounted at both extents of the piston position to prevent over-extension. Buoyancy engine cost was prioritized over energy efficiency, a trade-off deemed acceptable since our observational focus was dynamics over short time intervals (< 1 day).

The nominal volume of the float with the piston fully retracted is 4700 cm^3. Fully extended, the piston increases the volume by 450 cm^3 ($\pm$ 10 cm^3 due to manufacturing variability), providing a 9% change in total displaced volume. Floats are ballasted to be within 50 g of neutral buoyancy with their piston halfway extended in fresh water and have an approximate mass of 4.9 kg. While not strictly necessary, we add calibrated weights when deploying in salt water to maintain balanced bidirectional performance of the buoyancy engine.

The μFloat is controlled by a single-board computer (Beaglebone Black) running a Linux-Debian operating system that runs mission control, sensor telemetry, and data acquisition. Programming and data offload occur via WiFi when on the bench or on-board the vessel. All system status and sensor data are recorded continuously to a 32 GB micro SD card. A GPS receiver (Adafruit) provides position and pulse-per-second (PPS) clock synchronization while on the surface. For recovery, coordinates are transmitted to a support vessel via redundant 900 MHz RF radio (XBee) and cellular (Particle Electron) modems. These communication methods also permit the exchange of short data messages and commands between floats and the support vessel, such that floats can be re-tasked without physical retrieval. For underwater communication and localization, we utilize nanomodems (Fenucci et al., 2018; Neasham, 2016), an inexpensive ($\sim$ \$250 US) underwater acoustic modem (further details in Section 4.2). An onboard inertial measurement unit (IMU) also records orientation and acceleration (translational and rotational). To date, the IMU data has only been used for diagnostic purposes (e.g., identifying seabed contact), however we anticipate adding inertial navigation between acoustic position updates to improve localization accuracy and resolution. Additional USB, serial, analog, and I^2C connections are available for auxiliary sensor integration. The top end cap hosts all of the external interfaces and components. These comprise a pressure sensor (Honeywell) and temperature sensor (BlueRobotics). The GPS patch antenna, nanomodem acoustic transducer, and RF and cellular antennas are potted in a single, custom unit. Additionally, a charging plug, vent plug, auxiliary port and power switch are all also located on the top end cap. Power is provided by a rechargeable Li-ion battery pack with 100 W-hr capacity. The hotel load consumes between 3-5 W, resulting in a maximum endurance of 20-30 hr.

3 Buoyancy Control Implementation and Evaluation

Active control of the μFloat buoyancy engine is necessary to efficiently reach target depth and to maintain that depth under environmental disturbances. Overall, we prioritized isobaric/depth control, rather than Lagrangian vertical behavior, to ensure vertical distribution of the swarm throughout the water column.

3.0.1 μFloat Buoyancy Control

Control of the μFloat buoyancy engine is executed in software using feedback from the pressure sensor to achieve isobaric control. For simplicity, we will refer to this as "depth control", noting that pressure in dbar and depth in m are interchangeable within an accuracy of 3%

(i.e., maximum 3 m difference at 100 m rated depth). Prior to deployment, a predefined schedule of target depths and durations is constructed. Using a graphical-user-interface (GUI) developed in MATLAB (Mathworks®), the schedule is uploaded to floats via WiFi.

During a dive sequence, depth control is achieved via a closed-loop two-stage cascaded proportional-derivative (PD) controller operating based on both float depth z and vertical velocity v (Fig. 3). Float depth is provided by the pressure sensor sampling at 10 Hz. The raw data is smoothed using a fourth-order digital Butterworth filter. Float velocity is computed via a digital differentiation of the filtered pressure signal. The filter introduces a one-second lag in both depth and velocity observations. In the first stage of the controller, the position error (target minus current depth) is calculated. From this error, a recommended velocity is computed based on PD_z gains and checked against a user-defined upper speed limit (V_{limit}) to determine a target velocity. In the second stage, velocity error (target minus current) is computed and the output motor command (with checks for minimal and maximal values) is calculated based on PD_v gains. To mitigate errors due to absolute drift of the pressure sensor ($< \pm$ 0.5 dbar/hour, $\pm$ 1 dbar max), ambient pressure is sampled whenever the float surfaces and dive pressure (depth) is computed relative to the most recent surface pressure. Gains (PD_z and PD_v) were manually tuned to minimize time to target depth and maximize depth-holding stability in a series of shallow water laboratory trials. These gains were held constant for subsequent testing. As shown in Figure 4, the velocity limit (V_{limit}) improves transient dynamics, as well as enabling constant-speed profiling modes.

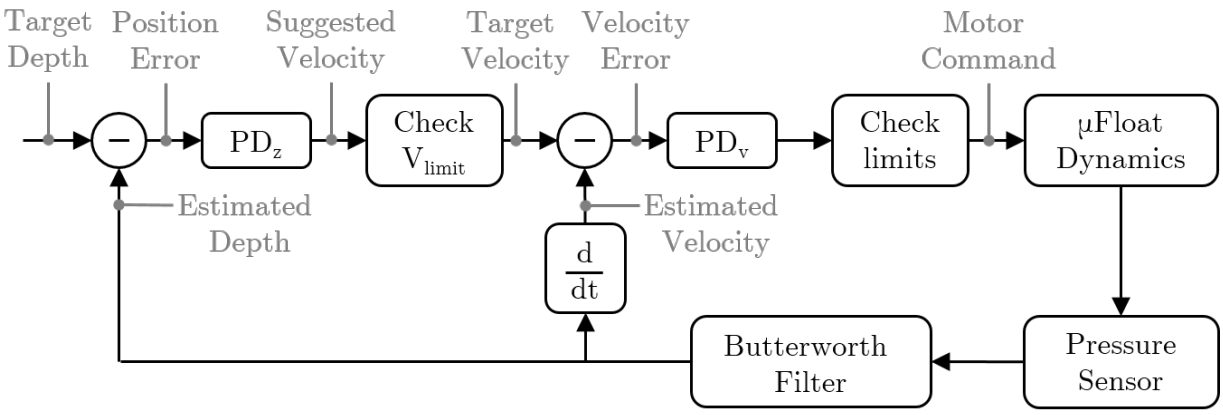

Figure 3: Block diagram of μFloat depth control. Control scheme is closed-loop, two-stage, cascaded proportional-derivative (PD) controller with feedback from the pressure sensor. Inputs are target depth and velocity limit V_{limit} for constraining vertical speed.

3.1 Buoyancy Control Testing

Quiescent-flow field tests were conducted on 27 July 2020 in Lake Washington, WA, a large freshwater lake with a muddy bottom and a depth of 30-65 m in the testing region. Winds were light (1-2 m/s) and varied from SE to S over the course of the day. Depth control was evaluated during the first of two test periods, which lasted approximately 2.7 hours.

μFloats were deployed with a pre-programmed depth schedule designed to evaluate the buoyancy engine's transient dynamics and depth-holding accuracy, as well as float compressibility. The lake depth permitted control assessment over approximately half the float range, with target depths varying from 2.5 m to 42.5 m. The velocity limit control parameter (Fig. 3) ranged from 0.2 m/s (slow) to 1.0 m/s (effectively unrestricted, given the float terminal velocity of $\sim$ 0.5 m/s).

During this test, several μFloats were equipped with external sensors to provide supplementary data sets and to demonstrate adaptability. Four floats were equipped with hydrophones for acoustic assessment of nanomodem transmissions (see Section 4) and three floats with cameras (GoPro Hero 6 and Session 5) for visual examination of float performance.

3.2 Evaluation of Depth Control

3.2.1 Data Analysis

To distribute floats throughout the water column, the buoyancy engine controller must be able to efficiently bring a float to a target depth. To characterize depth control performance, the dive sequence was parsed into actions (any move from one target depth to another). From each action, we computed the following metrics: (1) settling time - the elapsed time between when the float moved 0.25 m from its starting depth to settling within 0.25 m of the target depth; (2) overshoot – the max deviation (m) from the target depth prior to settling; (3) depth-holding accuracy after settling, assessed as mean offset from target depth, and (4) deviations from the settled depth, assessed as the interdecile range of actual minus mean settled depths. Actions with steady-state periods less than 30 seconds were excluded due to lack of statistical convergence.

3.2.2 Depth Control in Lake Washington

The buoyancy control algorithm was able to successfully and consistently control float depth across a range of depths, as pictured in Fig. 4a. For a float starting on the surface with piston fully extended (e.g., Figs. 4g-k), it took $\sim$ 30 s to retract the piston past the neutral buoyancy position to begin diving. This must be accounted for when deploying in energetic environments to ensure the floats reach depth within the region of interest, either by deploying upstream of that region or by pre-retracting the piston. Floats have a $\sim$ 0.5 m/s terminal velocity (e.g., Fig. 4m, min. 125). The velocity limit, applied to adjust the dive speed of the float, proved effective at reducing overshoot when the limit was smaller than the terminal velocity (e.g., compare overshoot in Figs. 4b,g to Fig. 4l). While the unconstrained float (Figs. 4l-p) reached the target depth fastest, the additional time spent recovering from the larger overshoot resulted in a settling time similar to that of the float with a 0.2 m/s velocity limit ($\sim$ 180 sec), which conversely took longer to reach the target depth, but experienced minimal overshoot ($\sim$ 2 m).

Extracting depth performance statistics from all float dives taken in Lake Washington (Fig. 5,

colored circles), we find that overshoot can vary from < 1 m to 14 m depending on target depth and the velocity limit. For purposes of dive planning, the average settling time is roughly 10 s + 4 s per meter of target depth, an effective average dive velocity of 0.25 m/s. Increasing the effective dive velocity would require a more advanced control strategy (e.g., model predictive control). Floats are able to hold depth to within the absolute accuracy of the pressure sensor (($\pm$ 1 dbar; Fig. 5c), with deviations around the settled depth < 0.2 m (Fig. 5d). While such transient and steady-state performance is desirable, it is achieved at the cost of near-continuous actuation of buoyancy engine (Figs. 4e,j,o), increasing power consumption (Figs. 4f,k,p). A velocity limit ≤ 0.5 m/s improves consistency of both settling time and overshoot across variably ballasted floats (Figs. 5a,b), but does not influence the depth-holding characteristics of the float (Figs. 5c,d). Lastly, variations in buoyancy control dynamics due to the attachment of modestly-sized auxiliary sensors (i.e., hydrophones and GoPro cameras, $<$10% V_o) are indistinguishable from variations across standard floats and thus do not require any special control tuning.

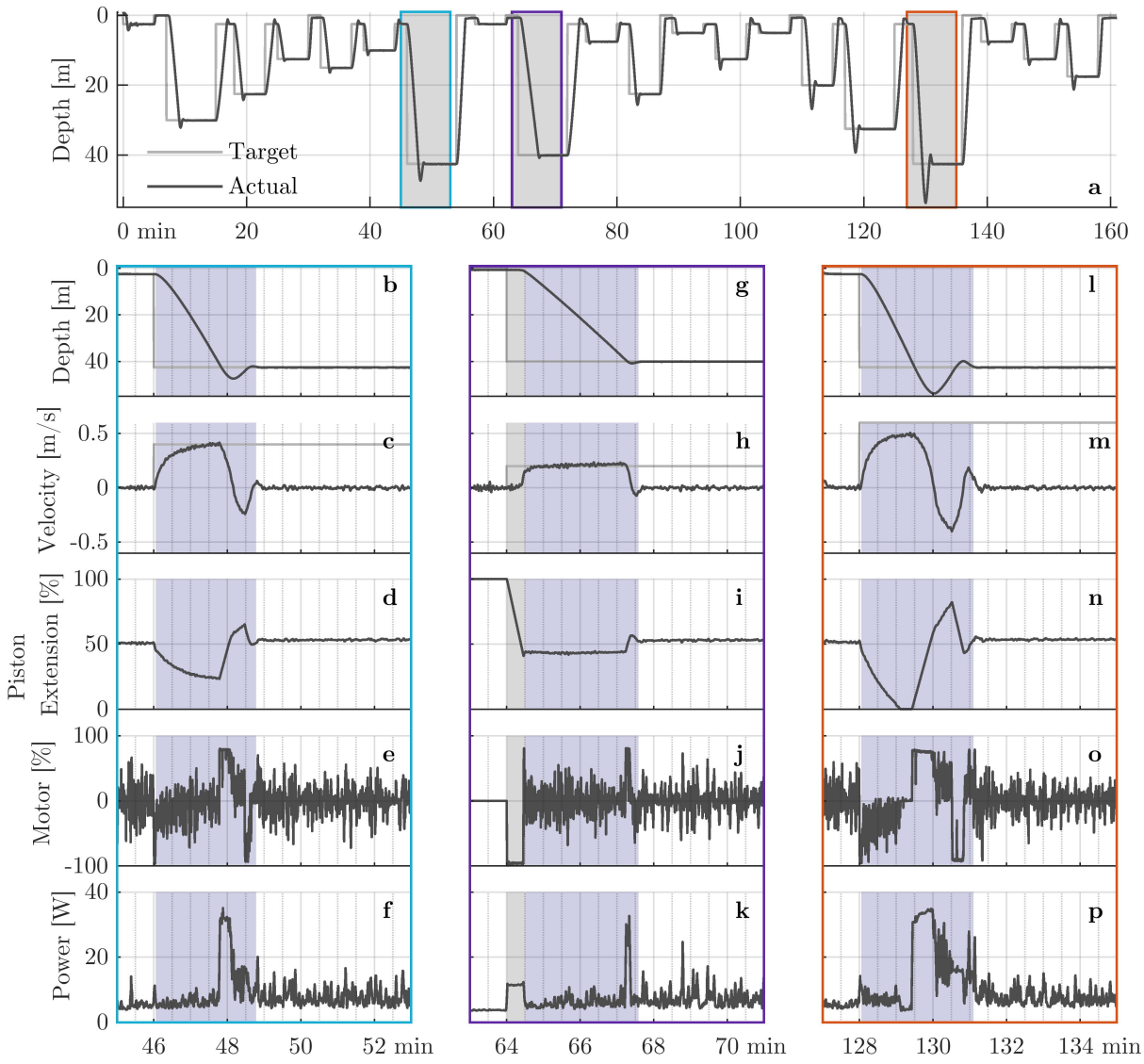

Figure 4: Depth control of uFloat 009 during Lake Washington - Test 1 (a). Three dives are highlighted, with detailed characteristics pictured in (b-f), (g-k), and (l-p). Velocity limit for each dive was 0.4 m/s (b-f), 0.2 m/s (g-k), and 0.6 m/s (effectively unconstrained, l-p). The grey region in (g-k) highlights the piston retraction period for a dive initiated from the surface. The settling period is highlighted in purple (b-p).

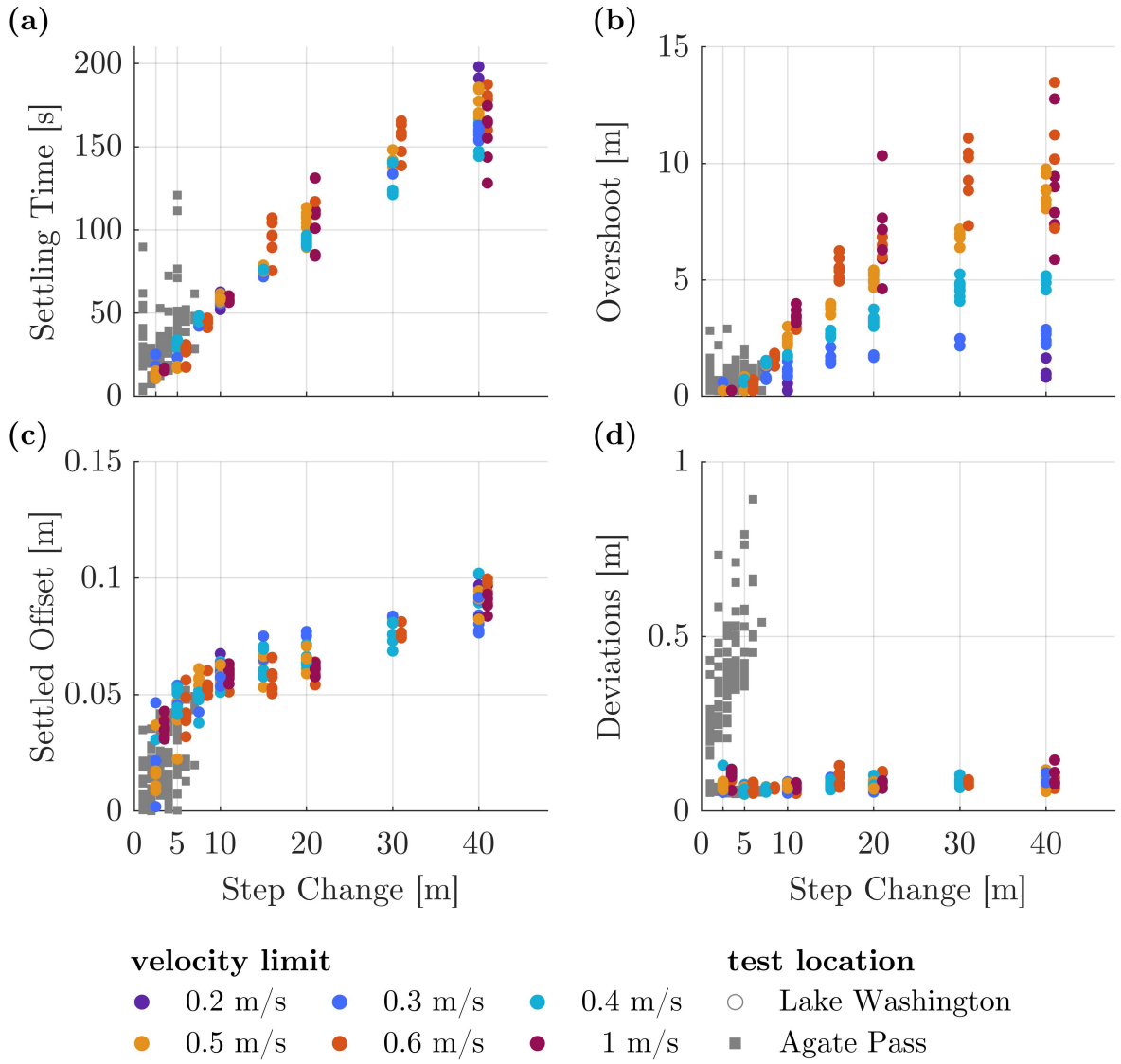

Figure 5: Fleet-wide statistics for depth control actions during Lake Washington (circle) and Agate Pass (square) tests. All Agate Pass floats were programmed with a 0.3 m/s velocity limit. 0.5, 0.6, and 1 m/s velocity limit data points from Lake Washington include an offset (1 m) on the horizontal axis to facilitate visualization.

3.3 Evaluation of Float Compressibility

While the depth control accuracy achieved was well within the design requirements, the motor moved more frequently than expected given the quiescent conditions in the lake. Once the float has reached neutral buoyancy (i.e., its density matches that of the surrounding water), its stability should primarily depend on its compressibility relative to the compressibility of water, as any difference will generate a relative change in buoyancy if perturbed from the settled depth. If the float is less compressible (stiffer) than water, a restoring force results, returning the float to the original depth, or more precisely, the original isopycnal (D'Asaro, 2017). If the float is more compressible than the surrounding water, neutral buoyancy is a dynamically unstable state and the float must actively control its density to maintain a desired depth or isobar. For such a float, passive isobaric control and Lagrangian/isopycnal control requires stratified water. But even though the μFloats are expected to be more compressible than water due to the housing, the resulting forces are expected to be small and produce accelerations on the time scale of minutes, rather than the seconds observed in the motor behavior.

To better understand the impact of float compressibility on dynamic stability, we characterized compressibility by examining how the neutral-buoyancy piston position – the average position of the piston when holding depth – changed with hydrostatic pressure. A decrease in nominal float volume V_o due to compression increases the nominal density (given a constant float mass). Thus, to maintain neutral buoyancy, the piston must extend to compensate for the lost nominal buoyancy. Accordingly, we assessed float compressibility γ by computing the difference between neutral buoyancy piston volume V_{piston} at 2.5 m (reference depth, z_{ref}) and the piston volume for neutral buoyancy at greater depths z, normalized by the nominal float volume V_o, and accounting for the change in water density with depth $\rho(z)$ produced by the thermocline (Fig. 8b). That is,

$$\gamma = \frac{1}{\Delta p}\frac{\Delta V}{V} = \frac{V_0(\frac{\rho(z_{ref})}{\rho(z)} - 1) + V_{\text{piston},z_{ref}}\frac{\rho(z_{ref})}{\rho(z)} - V_{\text{piston},z}}{(p(z) - p(z_{ref}))V_0}.$$

To interpret float compressibility in the context of water compressibility or stratification, we cast compressibility into a change in nominal float density $\Delta\rho_{nominal}$ with hydrostatic pressure, assuming a reference water density $\rho_{ref} = 1000$ kg/m^3 – fresh water at 15 °C, following

$$\Delta\rho_{nominal} = \gamma * \Delta p * \rho_{ref}.$$

This analysis reveals that the floats are significantly more compressible than water (Fig. 6), though only about 1/3 of the loss in volume can be attributed to the compression of the cylindrical housing shell (following Roark et al. (1976)). The remainder is hypothesized to be trapped air exposed to ambient pressure, since the shallow and short dives are likely insufficient for dissolution of entrained air and surface bubbles (D'Asaro, 2003).

This high relative compressibility means that in well-mixed or weakly-stratified waters the float is isopycnally unstable, and thus requires frequent actuation to maintain a target depth.

If deployed in a stably stratified environment, the water density gradient will counteract float compressibility. Results from Lake Washington indicate that the minimum stratification necessary for isopycnal operation is approximately $\delta\rho/\delta z > 0.00015$ (g/cc)/m, or about 0.2 PSU/m salinity gradient. While the μFloat would ideally be less compressible than water to enable passive depth control, this would require a more expensive housing, running counter to the design specification to minimize cost.

Lastly, the question remains whether dynamic instability due to float compressibility drives the near-continuous motor movement. Based on the characterized compressibility, if a μFloat with piston extended such that it is neutrally buoyant at 40 m is offset from that depth by 0.1 m, it would take $\sim$ 1 minute to move another 0.1 m distant. While of similar magnitude, the movements around the settled depth occur on the order of 10 s, much faster than can be attributable to the compressibility. As such, we believe the current control algorithm (Fig. 3), while decently tuned for the transient performance, is overly sensitive when holding depth and the primary cause of the near-continuous manipulation of the buoyancy engine.

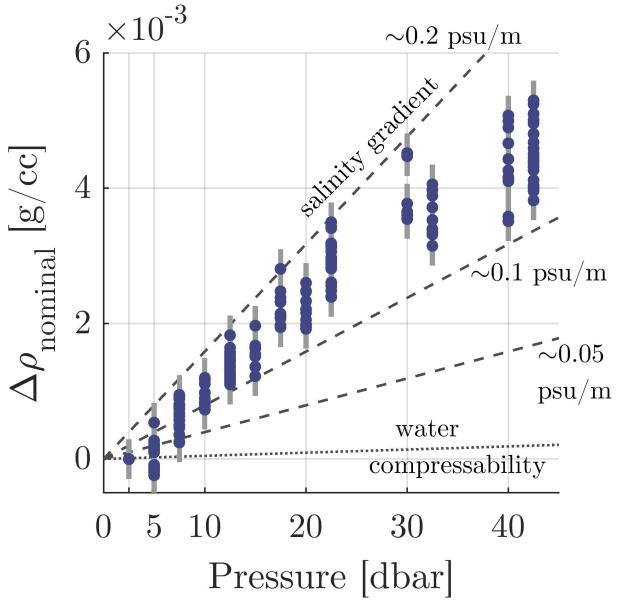

Figure 6: Equivalent change in float density with pressure due to compressibility. Points indicate an individual measure of float compressibility. Vertical grey bars indicate confidence intervals based on piston position uncertainty. Water density changes due to compressibility (for fresh water at 15 °C, dotted line) and vertical salinity gradients (dashed lines) are included for reference.

4 Underwater Localization Implementation and Evaluation

4.1 Design

Design of the underwater localization system was motivated by the desire for high-resolution float trajectory data, from which horizontal velocity could be reliably extracted. While GPS provides float position while on the surface, the signal does not penetrate subsurface. As with the buoyancy engine, we prioritized an inexpensive localization solution.

4.2 Implementation

For subsurface positioning, we utilize a network of Surface Localization Buoys (SLBs) equipped with acoustic nanomodems (Fig. 7a). A minimum of three SLBs, either moored or drifting, provide a long-baseline style localization architecture (Smith and Abel, 1987). Surface buoy electronics are a simplified subset of the μFloat's contained within an acrylic housing (Blue Robotics). The external structure consists of buoyant yellow foam upper and a subsurface spar (1 m long) from which the nanomodem transducer extends.

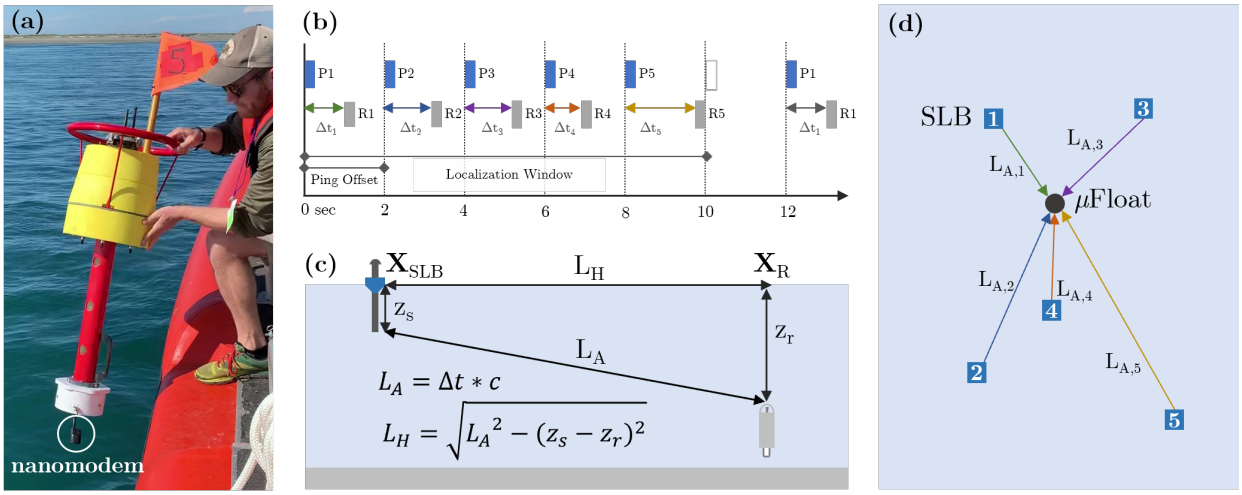

Figure 7: Localization architecture: a localization buoy (SLB) being deployed by the first author (a); nanomodem ping scheduling (b); computation of the horizontal distance L_H from the time of flight (c); plan view of the localization array (d).

The nanomodem (v2) is a low-cost acoustic modem ($\sim$ \$250) that exchanges messages on a carrier frequency band of 24-28 kHz. They have a maximum data rate of 40 bit/s, a source level of 168 dB re 1 μPa 1 m, and a nominal range of 2 km (Fenucci et al., 2018; Neasham, 2016). Nanomodems were chosen as they met the communication requirements necessary for underwater localization at significantly lower cost (10x) than other commercially available acoustic modems. When integrated, the nanomodem was still under development and

the version of the hardware used could not parse overlapping messages and thus a time-division-multiple-access (TDMA) approach was used to schedule SLB localization pings. All nanomodems within broadcast range (i.e., both those on subsurface μFloats and on nearby SLBs) recorded and timestamped received pings.

Positional information was determined in post-processing, after data have been off-loaded from both the μFloats and SLBs. The sent and received pings are aligned to calculate the time-of-flight, and estimate the corresponding range based on a measured or assumed sound speed (Fig. 7c). Three or more range estimates occurring within the round-robin time are combined to trilaterate the μFloat positions with a least-squares fit (Norrdine, 2012). The resulting localizations are intermittent, noisy, and can indicate physically unrealistic float motion. Egregious outliers (e.g., positions on land) are removed and remaining data are smoothed using a robust (outlier-rejecting) locally-weighted, quadratic regression (MATLAB 'smooth' function with 'rloess' option). For a given track, the smoothing window was chosen programmatically to ensure sufficient observations were used in the regression. Windows varied from 60 to 240 seconds with 60 second discretization. Finally, to estimate velocity along the track, we apply a first-order central-difference scheme to the previously smoothed data. Additional details on localization processing are provided in Harrison (2021).

It is important to note that this time-stamped approach depends on synchronized clocks. Both SLB and μFloats clocks are synchronized to the GPS pulse-per-second output while on the surface. When subsurface, the μFloat clock (crystal oscillator on the onboard computer) has a maximum drift of 30 parts-per-million, such that after 30 minutes underwater, the maximum offset expected is 0.054 s. Additionally, the assumption of negligible float movement between pings depends on the ping offset and water velocity. For example, if the horizontal float velocity is 2 m/s and the ping offset is 1 second, float position may change up to 6 m in the time required to receive all three pings in a localization set. This effect can degrade the benefits of over-determined localization using more than three pings.

4.3 Testing of the Underwater Localization System

The underwater localization system was evaluated during the μFloat testing in Lake Washington described in Section 3.1. Two test periods occurred, with layouts as pictured in Fig. 8. Five SLBs were deployed during both tests, scheduled with a 2 s ping offset. Prior to Test 1, profiles of water density and sound speed were measured (Valeport miniSVP), revealing a strong thermocline (Fig. 8b).

Test 1 (LW-1) lasted approximately 2.7 hours and evaluated connectivity and accuracy. As such, three SLBs were deployed in an equilateral triangle ($\sim$200 m on edge) around the floats to provide consistent localization data throughout the experiment. Two additional SLBs (4,5) were initially deployed about 1600 m distant and moved sequentially closer to the floats over the course of the two-hour deployment. To better understand acoustic conditions impacting nanomodem connectivity, four μFloats were deployed with an externally mounted hydrophone (OceanSonics icListen HF).

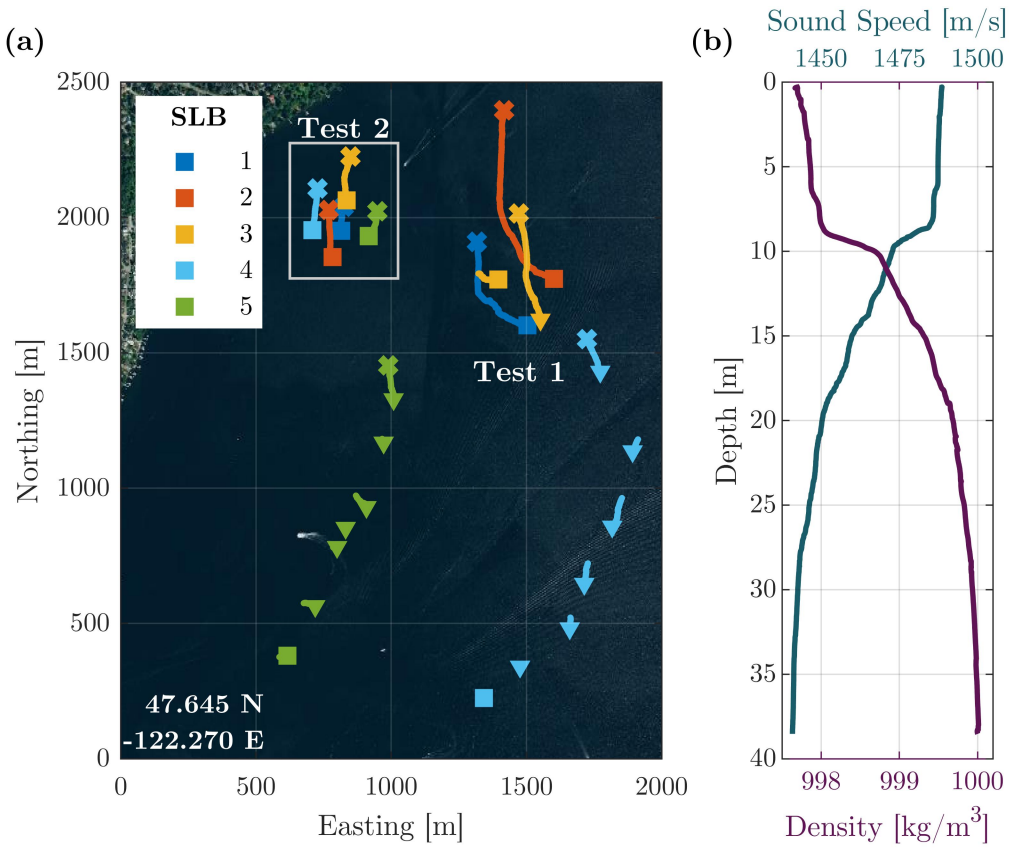

Figure 8: Layout of surface localization buoys (SLBs) (a) and sound speed and density profiles (b) during Lake Washington tests. ■ and ✖ mark the starting and final locations, respectively, for each test. Some SLBs were manually relocated during Test 1, with ▼ marking each new starting location. Twenty μFloats were deployed in the center of the triangle formed by SLB 1-2-3 in Test 1, and two floats nearly collocated with SLB 1 in Test 2. SLB movement was wind-driven, with light wind (1-2 m/s) varying from SE to S over the course of the day.

Test 2 (LW-2) lasted approximately 30 minutes and evaluated optimal localization accuracy, with all five SLBs deployed in a cross configuration, with a maximum separation distance of 300 m. To assess horizontal position uncertainty, two μFloats were programmed to sit on the lake bottom for fifteen minutes, thus acting as stationary targets, following Casagrande et al. (2019). An additional four floats were deployed at depths varying from 2 to 10 m, but their data was utilized only in connectivity analysis.

4.4 Evaluating Nanomodem Connectivity

4.4.1 Nanomodem Connectivity Analysis

Underwater localization relies on the receipt of pings from a minimum of three surface buoys within the localization window (e.g., 12 s in Lake Washington) and is thus impacted by the

underlying connectivity between source and receiver. We evaluated connectivity as the ratio of pings received from an SLB relative to the total possible.

To evaluate how connectivity was impacted by acoustic conditions, data from the μFloat-mounted hydrophones were processed in MATLAB (Mathworks®) to extract pressure spectral density levels over the duration of the test. We calculated the 10-second moving-median sound pressure level within the 24-28 kHz transmission frequency band as a measure of ambient noise. Pings appeared as short, distinct elevations in this band, and were identified using a matched filter. The received level for each ping was calculated as the root-mean-square band level over the duration of the ping. Subtracting the ambient noise level from the received level (in dB space) provided a signal-to-noise (SNR) ratio for each ping in the hydrophone data stream. The hydrophone time series was manually aligned to μFloat time series by reference to both the nanomodem ping record and μFloat buoyancy engine motor noise. The nanomodem pings recorded on the hydrophone were then labeled with their corresponding source SLB by reference to the known ping schedule. μFloat depth and transmission distance for each possible ping were extracted from the μFloat data series. Additional details on acoustic processing can be found in Harrison (2021).

4.4.2 Nanomodem Connectivity Performance

In general, nanomodem connectivity rates are expected to decrease with decreasing SNR, however the cutoff within which receptions can be expected (i.e., connectivity rates $> 50\%$) must first be determined before assessing the relative impacts of propagation losses (e.g., spreading and absorption) and elevated background noise (e.g., vessel traffic). To do so, we binned all Lake Washington pings into 5 dB levels (Fig. 9) and computed the ratio of received to possible pings. Levels for missed pings were estimated via interpolation from temporally adjacent received pings from the same source. As expected, connectivity was strongly correlated with ping SNR, with reception rates near 100% for SNR > 30 dB and reducing roughly linearly down to 0 dB, at which point reception rates were effectively 0% (Fig. 9a).

To disambiguate the impact of range, receiver depth, and elevated background noise, we examined how nanomodem connectivity varied with depth and distance (Fig. 10a). High reception rates ($> 75\%$) are observed within 400 m, followed by rapid deterioration with distance and a maximum range of ~ 1000 m. This range is slightly shorter than expected: the nanomodem source level is 168 dB and average noise levels in the carrier frequency band were roughly 75 dB, indicating a maximum allowable propagation loss of ~ 90 dB. Near-field (< 60 m) receptions exhibit 45-55 dB SNR, corresponding to a loss of 35 dB in the first 60 m of transmission, which matches spherical spreading. Theoretically, the remaining 55 dB could provide > 10 km range, assuming < 1 dB/km loss due to absorption in fresh water and cylindrical spreading, but the observed range was significantly smaller.

The diminished nanomodem range was partly due to the downward refraction due to the strong thermocline (Fig. 8b) present on the day of testing. Comparison of the acoustic path distance to GPS-based source-receiver distance revealed a significant percentage of pings

on both SLBs and μFloats with time-of-flights corresponding to a propagation path that included a bounce off the bottom (Table 1). Flagging these pings and plotting by depth and distance, we see that nearly all receptions outside 375 m likely included a bottom bounce (Fig. 10b). Received levels for direct paths are 5-15 dB higher than bottom bounce paths of the same acoustic path distance. This attenuation range is consistent with expectations for bounces of varying grazing angles off a soft muddy bottom (Jackson et al., 2010). The impact of refraction is also evident in how connectivity (Fig. 10a) and SNR (Fig. 10c) change with receiver depth. Within 375 m, deeper receivers maintaining higher reception rates and SNR at longer ranges. Beyond 375 m, bottom bounce effects dominate.

Nonetheless, the nanomodems have proven effective at SNR as low as 0 dB in previous deployments, so the degradation in connectivity from 30 to 0 dB observed here was worse than expected. Examination of the hydrophone records revealed that, as range increased, the channel also exhibited a severe multipath response composed of multiple arrivals as shown in Fig. 10e, as compared with the strong peak in the near-range (d). Here, a perfect signal has one peak of magnitude 1 and a signal with very low SNR has will have a low peak value. However, a signal with high SNR and lot of multipath with also show low correlation. Pings sent from similar distance as (e) that were observed on the hydrophone record but not recorded by the floats exhibited even more dramatic multipath signals. This greatly increased the probability of missing receptions and the probability of locking onto a reflected path rather than the earliest path. Thus, the performance reported here is representative of severely unfavorable acoustic conditions.

While elevated background noise is another possible cause of reduced range, vessel traffic (the primary contribution during testing) increased background levels in the transmission band by roughly 10-20 dB for short periods (1-2 minutes), and thus deemed insignificant relative to the propagation losses discussed here.

The significance of propagation losses due to range, receiver depth, bottom interactions, and multipath signal degradation is borne out when comparing connectivity statistics for all μFloats and SLBs (Table 1) across the Lake Washington tests. Test 1 experienced lower SLB receptions, due to the lengthy period SLBs 4 and 5 spent at far range (> 750 m) from the other three SLBs. Connectivity improved dramatically during Test 2, as all SLBs were placed within 200 m of each other and the floats. μFloat connectivity matched this trend for the same reasons. Additionally, because the thermocline favors targets at depth, the μFloat reception rates were significantly higher and suspected bottom interaction rates significantly lower than those of the SLBs.

4.5 Evaluating Localization Accuracy

4.5.1 Analysis of Localization Accuracy

The ultimate purpose of the nanomodem array is to accurately estimate the horizontal positions of subsurface μFloats. Because the true location of the floats is unknown while underwater, system accuracy was assessed by examining acoustic localizations of the SLBs,

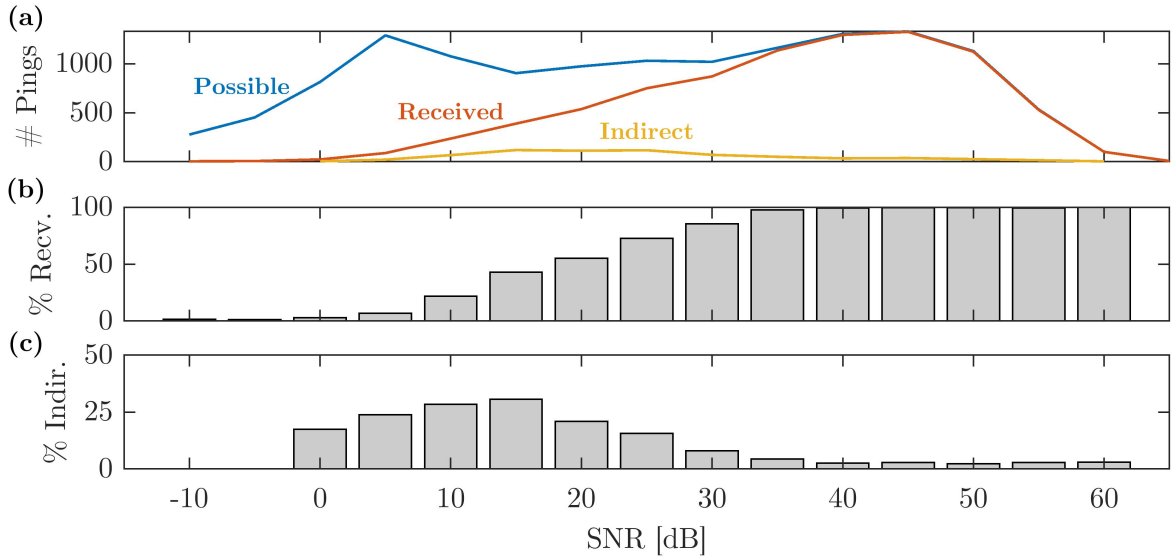

Figure 9: Received messages by SNR. This includes only data from the four μFloats with externally mounted hydrophones. (a) Total number of possible receptions, actual receptions, and suspected indirect paths; (b) Received percentage relative to total possible; (c) Indirect (i.e. transmission with suspected bottom interaction) percentage relative to total received. Bins with fewer than 20 receptions (less than 0 dB) are omitted.

as compared to their 'true' GPS data. From this standpoint, the SLBs are functionally equivalent to μFloats holding depth at 1.5 m.

To generate the 'true' position reference for all SLBs, their raw (1 Hz) GPS data was smoothed using a low-pass filter with 0.0167 Hz cut-off frequency (60 second period). A first-order central-difference scheme was applied to the smoothed position data to provide the horizontal velocity reference.

To isolate the influence of the source geometry on localization accuracy, we also applied the localization algorithm using the GPS-measured distances between source and receiver SLBs as the range inputs in the trilateration process (replacing the distances calculated from acoustic time-of-flight).

4.5.2 Accuracy of Underwater Localization

When SLBs received consistent pings, localization was possible and positions calculated from raw acoustic data generally matched GPS data, though with considerable noise (Fig. 11a). To correct for acoustic paths with suspected bottom bounces, we estimated the corresponding direct path distances by assuming a nominal water depth (60 m in Test 1, 30 m in Test 2) and a triangular path from source to bottom to receiver. Methods for identifying paths with suspected bounces and corrections are detailed in Harrison (2021). Correcting for bottom bounces reduced scatter, but did not eliminate it. Test 1 and Test 2 have similar position errors before correcting for bounces (Table 2), but the corrected values for Test 1 are twice

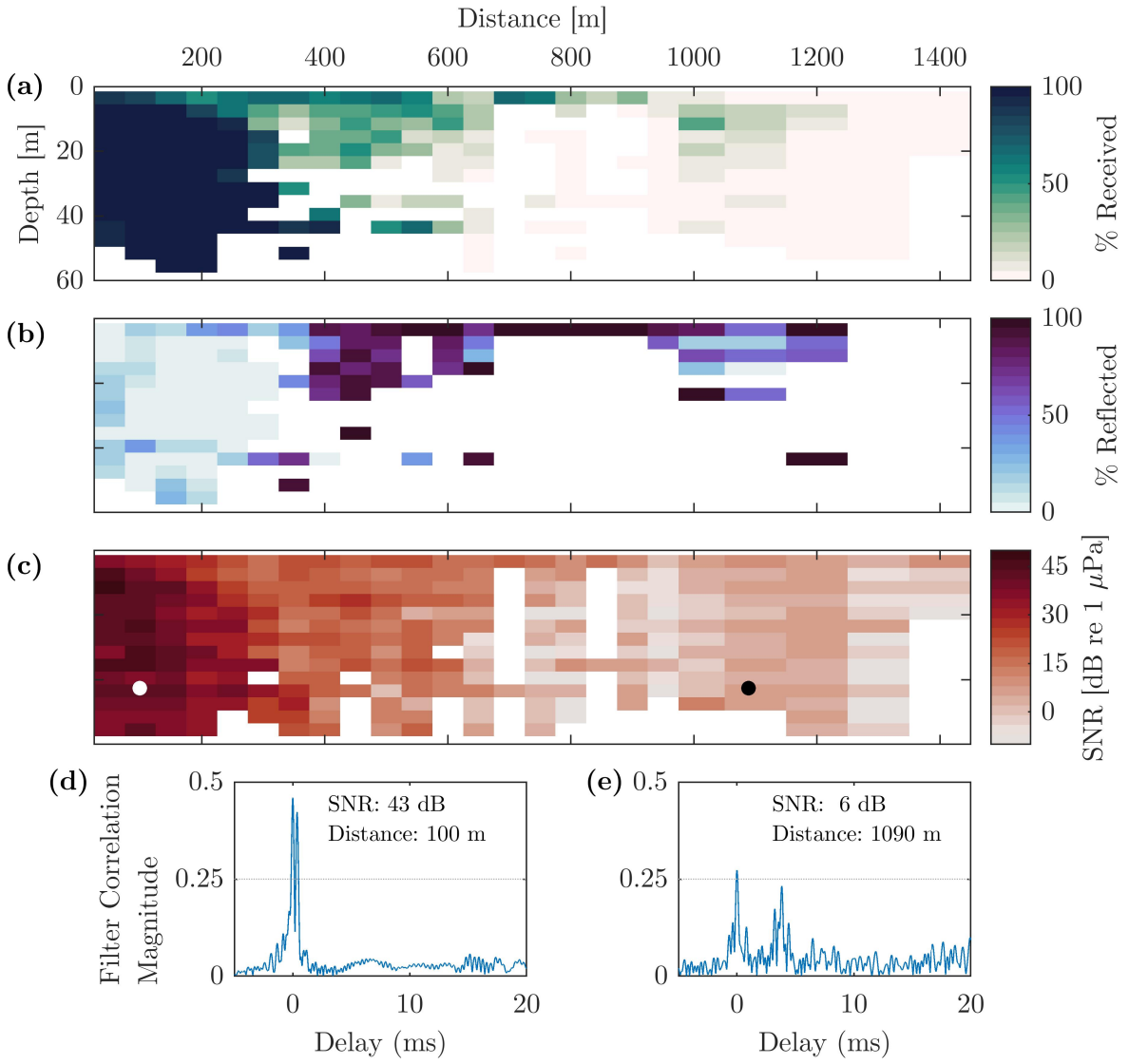

Figure 10: Nanomodem connectivity during Lake Washington as a function of depth and source-receiver separation distance. (a) overall percent received relative to possible receptions; (b) percentage of received messages suspected of being following an indirect path; (c) SNR of received pings. (d) and (e) show examples of the matched filter correlation strength used to identify the pings, centered on peak correlation time for each received ping. White and black marks on (c) correspond to (d) and (e), respectively.

as accurate as for Test 2. The likely cause is that Test 1 occurred over the main basin of the lake, where the nominal depth of 60 m was widely applicable. Test 2 (Fig. 11a) occurred over a sloped region of the lake, with depth increasing by 30 m from SLB 4 to SLB 5. Thus, the single nominal depth used to correct for bounces proved less effective. However, even after correction, positions remain noisy and indicate non-physical trajectories.

Smoothing the data produces physically realistic tracks. Position errors (50^{th} percentile) are within 4 m of the GPS positions in Test 1 and 8 m in Test 2 (Table 2). Artifacts do remain (e.g., excursions from GPS tracks for SLB 2, 3, and 5). To explore their source, we examined how the localizations improved if GPS-based distances were used in the trilateration process. The resulting estimates matched the GPS locations to within GPS accuracy (Table 2) in Lake Washington, which suggests that the errors in acoustic-based trilateration are a consequence of uncertainty in time of flight due to sound speed variations, ray path length, and bottom interactions, rather than unfavorable array geometry. We note that SLB to SLB connectivity was significantly lower than SLB to μFloat connectivity when floats were deeper than 5 m, with 57% of distance estimates requiring a bounce correction. Consequently, these errors should be interpreted as an upper bound on μFloat localization errors.

Localization of the two grounded floats during Test 2 provided a measure of position uncertainty in near-optimal SLB geometry. Uncertainty was 1.0 m, computed as the 68^{th} percentile Euclidean distance between instantaneous position estimates and the median position while grounded, with an approximately circular distribution. No pings received on the two grounded floats were suspected of following an indirect path (i.e., no bottom bounce). This uncertainty is similar in magnitude to GPS-trilateration accuracy and smaller than the accuracy of individual GPS position estimates ($\pm$ 2.5 m). This suggests error due to clock-drift over the dive is negligible. This uncertainty can be treated as the lower-bound on μFloat position accuracy for a single ping and, correspondingly, the lower limit of horizontal spatial scales resolvable by the μFloats, barring appeal to other sensor streams (e.g., the IMU).

Table 1: Overall nanomodem connectivity. Percentage received is relative to total possible. Percentage indirect (i.e., paths with a suspected bottom interaction) is relative to total received messages. Distance is the root-mean-square distance between source and receiver device for all possible transmissions during the indicated test.

		Possible	**Received**		**Indirect**		**Distance**
LW - 1	SLB	15 190	4788	32 %	2744	57 %	850 m
	μF	45 855	27 672	61 %	3538	9 %	650 m
LW - 2	SLB	3041	1950	64 %	1259	65 %	160 m
	μF	2982	2695	90 %	448	17 %	110 m
Agate Pass	SLB	4817	2160	45 %	0	0 %	280 m
	μF	13 812	7618	55 %	0	0 %	330 m

Table 2: Localization errors for SLBs in Lake Washington and Agate Pass. 50^{th} percentile position error (relative to GPS positions) and velocity error (relative to velocity computed from GPS positions) for SLBs in Lake Washington and Agate Pass. Nominal SLB velocities for each case are provided for context. For Lake Washington data, "raw" error statistics include localizations using paths with bottom interactions, while the "cleaned" statistics use corrected path lengths. No bounces were identified in Agate Pass. Subsequent filtering of the cleaned acoustic data produces "smoothed" tracks, for which the corresponding errors are reported. "GPS trilateration" errors are computed from localizations using GPS-based distances.

		Lake Washington		**Agate Pass**
	Data Type	Test 1	Test 2	
Position Error (m)	*GPS trilateration*	0.4	0.3	12.4
	Raw	13.4	14.2	N/A
	Cleaned	4.1	10.4	12.2
	Smoothed	4.0	8.0	5.0
Velocity Error (m/s)	*Cleaned*	0.08	0.14	4.4
	Smoothed	0.008	0.020	0.035
Nominal Velocity (m/s)		0.04 ± 0.03 m/s	0.07 ± 0.03 m/s	1.4 ± 0.7 m/s

Assessment of velocity accuracy during Lake Washington tests was challenging, as SLB movement was driven by light winds and their speeds were consequently low and variable. Nonetheless, the velocities estimated from the smoothed acoustic position data generally match those computed from GPS-positions (Fig. 11b), with errors < 0.05 m/s. Errors in velocity computed from instantaneous GPS-based trilaterations and cleaned but unsmoothed acoustic data are greater than the nominal water velocity (Table 2) and omitted from the figure for clarity. As with position data, we expect these errors to be an upper bound for measures of float velocity, given the lower connectivity rates on SLBs relative to μFloats.

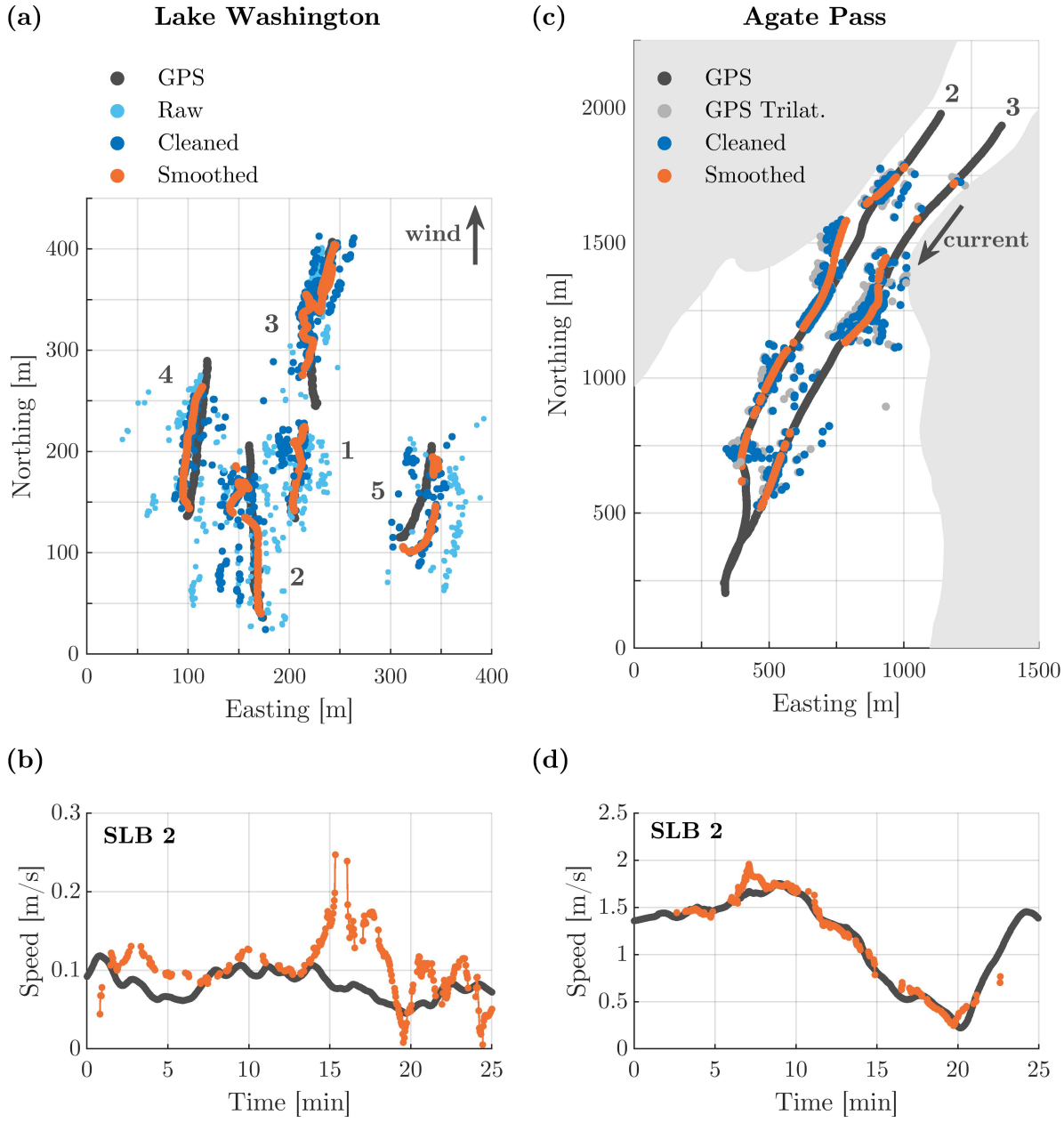

Figure 11: Localization system accuracy during Lake Washington - Test 2 (a,b) and Agate Pass (c,d). (a) and (c) compare acoustic localizations of SLBs relative to their known GPS positions. In Lake Washington, positions based on trilateration using GPS-estimated distances are indistinguishable from the true GPS track and omitted. In Lake Washington, "raw" localizations include calculations from paths with suspected bottom bounces, while "cleaned" data uses corrected paths. No acoustic bounces were apparent in the Agate Pass data, but localizations on land were "cleaned" (i.e. removed). SLBs are designated by number, with tracks from Agate Pass limited to SLB 2 and SLB 3 for clarity. (b) and (d) show velocity estimated from the smoothed acoustic position data (only at locations with valid position data) as compared to the velocity computed from the GPS tracks.

5 μFloat Swarm Demonstration

5.1 Field Deployment in Agate Pass, WA

The first full-scale scientific demonstration of the μFloat swarm was mapping horizontal water velocities in Agate Pass, WA, a tidal channel approximately 10 m deep and 300 m wide, with peak currents exceeding 1.5 m/s. On 20 August 2020, twenty floats were repeatedly deployed over an ebb-flood tidal cycle with a total of 9 survey periods, each with a duration of approximately twenty minutes. An example flood deployment is pictured in Figure 12. μFloat settings and SLB arrangements were determined by the primary objective of volumetrically characterizing the velocity field. Based on buoyancy control benchmarks from Lake Washington, a velocity limit of 0.3 m/s was implemented on all floats and floats were deployed roughly 60 m upstream of the region of interest to allow time for initial piston retraction. For a given survey, all floats were programmed to hold depth (depth targets varied from 1-10 m) or to repeatedly profile from the surface to depth (maximum depths varied from 3-10 m). Similarly informed by localization performance in Lake Washington, the following strategies were implemented in Agate Pass to ensure consistent localization: (1) SLBs were deployed within 500 m of the floats; (2) the ping offset was reduced to 1 second to increase the position update rate; (3) we avoided maneuvering the vessels near the floats to maximize SNR for localization pings. Auxiliary sensors on the μFloats were identical to those described for Lake Washington tests. GoPros were oriented looking downward and augmented with dive lights to survey the benthos, a rudimentary version of Roman et al. (2011). During each deployment, water density and sound speed were measured mid-channel, near the bridge crossing (Xylem CastAway CTD) and revealed minimal gradients (Fig. 12b).

5.2 Analysis of Swarm Deployment

While hydrodynamic mapping was primary objective of the Agate Pass tests, we first processed the data to investigate how μFloat system performance changed in an energetic environment. Float dives were analyzed using the same process as was used for Lake Washington tests (Section 3.2) to evaluate depth control performance. Due to the increased turbulence present in the channel, floats experienced significantly more vertical deviations than in Lake Washington. Thus, the 0.25 m tolerance threshold for defining the start of the settled period used in Lake Washington was relaxed to 0.5 m for Agate Pass dives. Note that all depth-holding tracks were included in the analysis, but profiling deployments were excluded.

Localization analysis followed the same process as Lake Washington tests. A comparison of GPS and acoustic path lengths indicated no distinguishable bottom bounces, which was consistent with the well-mixed, shallow (<10 m) nature of the channel. Analysis of localization accuracy in Agate Pass was restricted to a single flood deployment pictured in Fig. 12a.

For hydrodynamic mapping analysis, we assembled velocity data from all float tracks in the example flood survey period into a 3D linear interpolation function. A comprehensive analysis of velocity mapping and a comparison against other instruments (e.g., acoustic

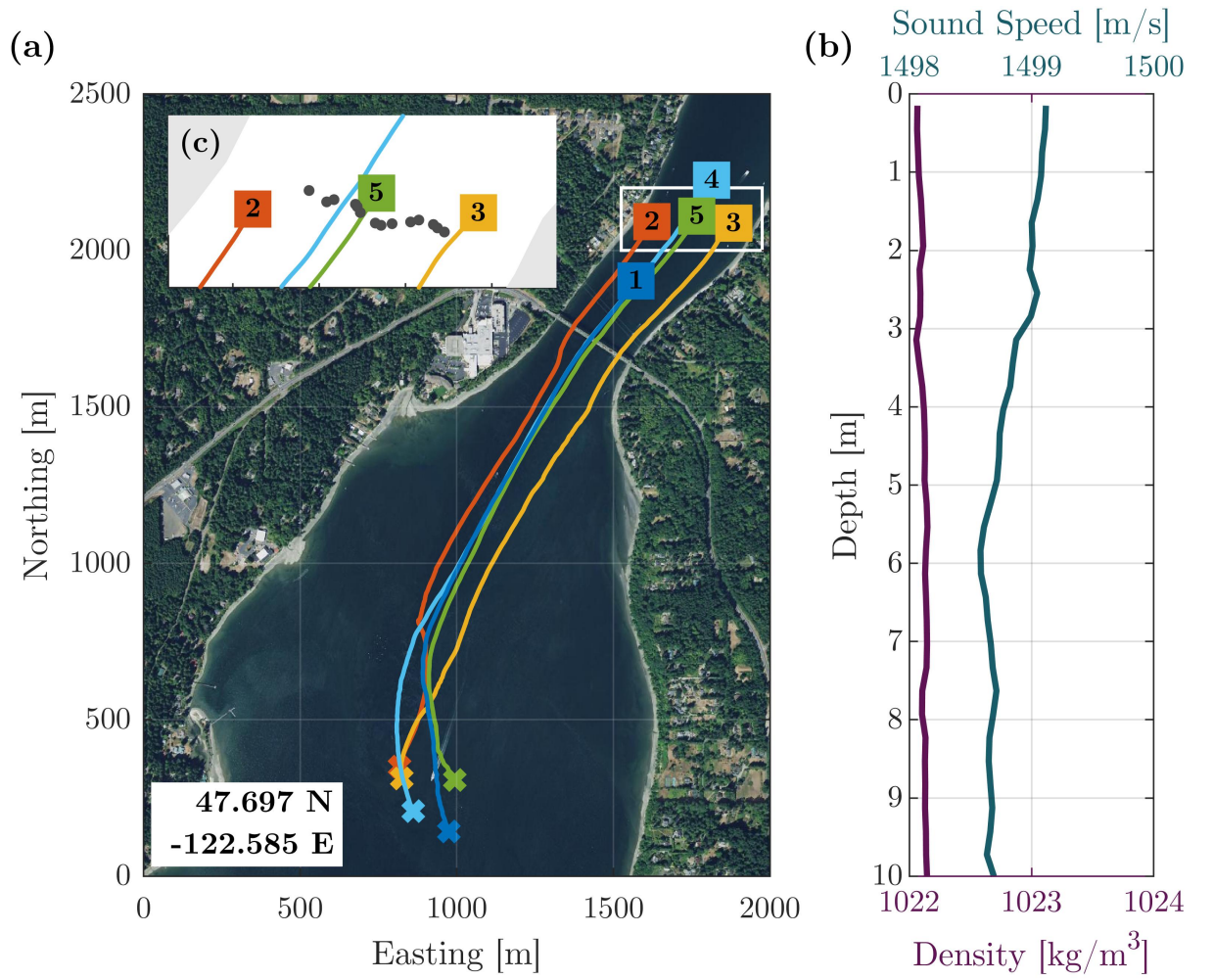

Figure 12: μFloat system deployment in Agate Pass during flood tide (a,c). Water density and sound speed as a function of depth during the test interval (b). ■ and ✖ mark the starting and final locations of the SLBs, respectively. μFloats, indicated by the grey dots in (c), were deployed moving westward from SLB 3 to SLB 2 and followed trajectories similar to the SLBs.

Doppler current profilers) will be included in a forthcoming manuscript.

5.3 Results

Swarm deployments in Agate Pass proved successful at mapping horizontal and vertical gradients of tidal currents, as observed in Fig. 13. By combining data along the trajectories of 18 floats (Fig. 13a), we observe an exit jet – a narrow region of high flow velocity extending out the southern mouth of the channel into the bay (Fig. 13b). Vertical profiles are typical of open channel flow (Fig. 13d). Also, the quasi-Lagrangian behavior of the floats revealed interesting secondary flow features, with three floats entrained in an eddy on the periphery of the exit jet (Fig. 13c).

System performance in Agate Pass was consistent with the quiescent benchmarks in Lake Washington. Floats were able to reach and maintain depths on operationally practical time scales, though some performance degradation was observed (and expected) due to the increased turbulence in the tidal channel relative to the quiescent lake. Settling time increased by about 10-20 s (Fig. 5a) and overshoot increased by 1 m on average (5b). Most significantly, deviations while holding depth were much higher (0.25 - 0.5 m).

Nanomodem connectivity fell between the two Lake Washington tests (Table 2). This follows the trend of source-receiver distance dominating connectivity effects, as the average separation distance during Agate Pass ($\sim$ 350 m) split the two Lake Washington deployments (500 m and 150 m). Ambient noise in Agate Pass was only only marginally higher than in Lake Washington (80 dB in the nanomodem communication band vs. 75 dB), Similarly, smoothed position errors for SLBs in Agate Pass fell between Lake Washington tests (Table 2), with 50% of position estimates within 5 m of the GPS values. However, examining the unsmoothed estimates revealed a different primary error source. SLB position errors based on trilaterated GPS-distances (12.4 m) were effectively equivalent to acoustic errors (12.2 m). Thus, accuracy degredation was more likely caused by poor SLB array configurations resulting from their freely-drifting and converging paths rather than properties of the acoustic environment. The faster currents in Agate Pass provided a better signal for evaluating velocity accuracy and revealed 50^{th} percentile velocity errors (0.04 m/s) that were less than 3% of the nominal flow speed (1.4 m/s).

6 Discussion

6.1 Buoyancy Control

The μFloat buoyancy engine demonstrated robust and accurate depth control in both quiescent and energetic environments, a prerequisite for maintaining vertical distributions when deployed in swarms. The large buoyancy engine capacity easily accommodated external sensors (hydrophones and GoPros), with only a rough re-ballasting (within $\pm$ 50 g) required to accommodate the extra weight and no adjustments to the controller necessary. The dy-

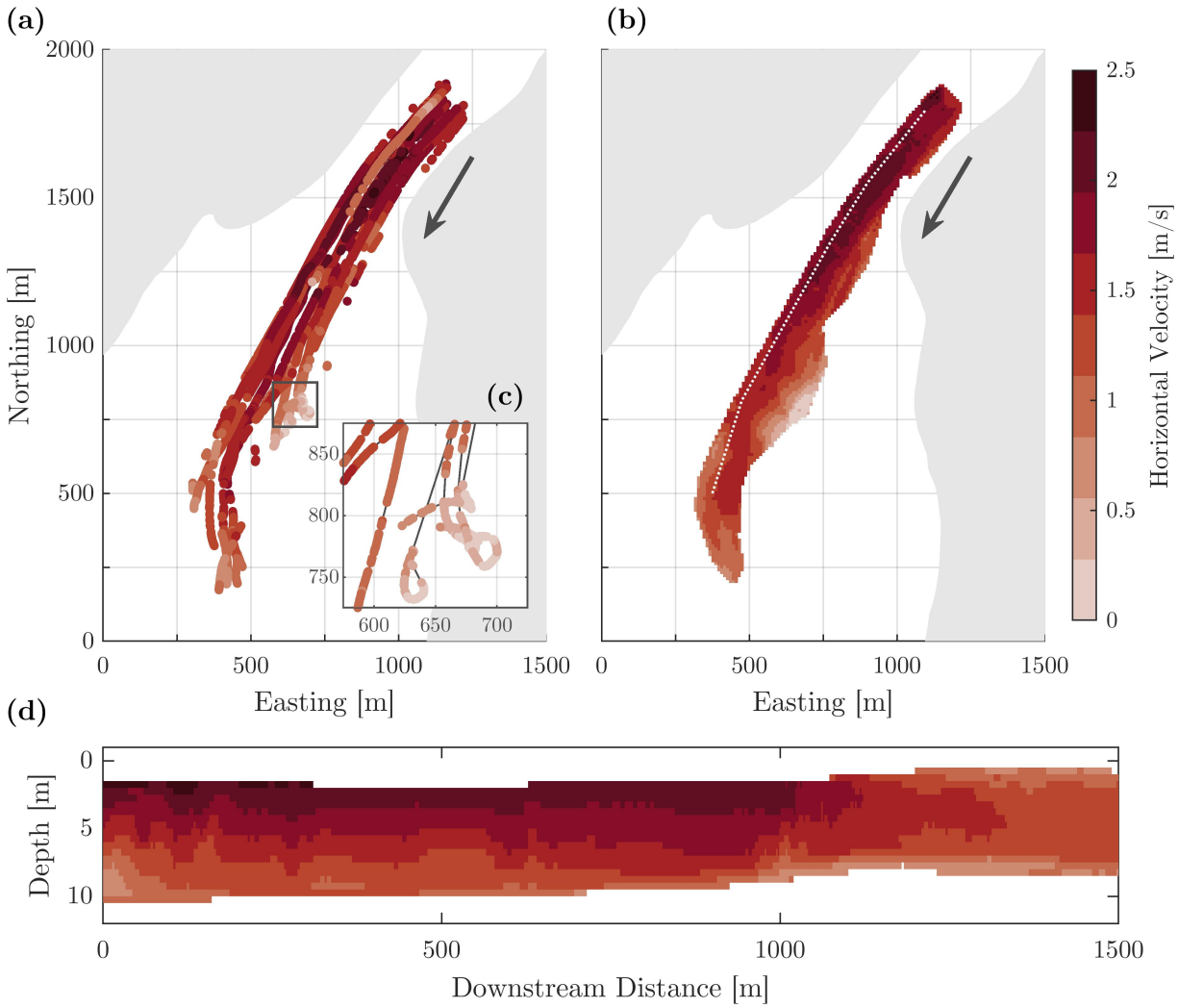

Figure 13: Horizontal velocity through Agate Pass during one flood tide survey. (a) depicts all float trajectories colored by instantaneous horizontal velocity. (b) depicts horizontal current speed interpolated over a plane at 3 m depth. (c) details float motion in an eddy off the primary exit jet. Tracks end when the floats resurface. (d) depicts the vertical structure of currents along the white line indicated in (b).

namics of floats with external sensors were indistinguishable from bare floats. In theory, the buoyancy engine could tolerate a 3x increase in float volume before losing the ability to accommodate an *in situ* density change from fresh to salt water, though any additional drag would decrease profiling speed and potentially impact operational strategies. For short duration deployments in high-flow conditions, understanding the μFloat's transient control dynamics is critical to planning effective swarm surveys. Here, implementation of a speed limit on float vertical velocity was effective at preventing undesirable overshoot and increasing the consistency of settling time across variably ballasted floats.

Testing revealed two potential improvements to the μFloat dynamics: reducing float compressibility and refining the software control algorithm. Due to the float being more compressible than water, it requires constant piston movement to maintain depth and precludes isopycnal control strategies except in strongly stratified environments. A stiffer housing material (e.g., aluminum) could help reduce actuation requirements, albeit at increased unit cost. Additional drag surfaces could also improve flow-following ability of the μFloat for applications where Lagrangian behavior is particularly critical (e.g., mixing studies (D'Asaro et al., 1996; D'Asaro, 2003)). Absent changes in housing composition, incremental improvements to the control algorithm could reduce the high-frequency motor action when holding depth.

6.2 Localization

The nanomodem-based localization array proved to be a robust, accurate, and inexpensive solution in quiescent and energetic environments. Nanomodem connectivity was sufficiently consistent to provide regular position updates and permit accurate calculation of float velocity. While an encouraging demonstration, the results suggest several areas of improvement, both in hardware and software.

In theory, the smallest time/length scales resolvable by the float are limited by float size ($O(10)$ cm) (D'Asaro et al., 1996; D'Asaro, 2003). In practice, resolution is limited by the update rate of the localization system. Here, the strict scheduling required for non-overlapping nanomodem messages restricted rates to 2 s in Lake Washington and 1 s in Agate Pass. Additionally, the variable nature of the acoustic channel results in noisy and gappy data, requiring smoothing to produce physically realistic float trajectories. Thus, the time window used in the smoothing operation limits the resolvable motions (20 - 60 s). It may be possible to overcome this programmatic limit by combining acoustic measurements with short periods of dead reckoning from IMU data (Caron et al., 2006) and thus approach the physical limit defined by the float size.

Improvements to localization accuracy are also possible. The two primary sources of error observed were (1) variations in sound speed and (2) poor SLB array geometry relative to receiving devices. The first was evident in Lake Washington, where the thermocline severely degraded path length estimates. Sound speed variation is a persistent challenge due to the variety of conditions exhibited in coastal waters. As such, errors and potential corrections must be addressed on a case-by-case basis. The significance of unfavorable array geome-

try was demonstrated in Agate Pass, where trilaterations using GPS-measured path lengths performed no better than those using acoustic path lengths. This could be improved by increasing the number of SLBs, mooring the SLBs, or even actively manipulating SLB distributions, either manually or by equipping autonomous surface vehicles with nanomodems. While insignificant for the short duration dives performed here, clock drift error may be an issue for longer dives. If so, solutions include occasionally surfacing to re-sync with GPS timing or using different localization algorithms (e.g., TDOA implemented by Neasham et al. (2021) or Bayesian methods employed by Raggi (2019); Casagrande et al. (2019); Thomson et al. (2019)).

Finally, an inverse localization architecture, with floats pinging to SLBs, would enable real-time monitoring of float positions. The directionality used here, with SLBs pinging floats, was dictated by the nanomodem scheduling requirement: a round robin TDMA cycle for the five SLBs was significantly shorter than it would be for twenty floats pinging to the SLBs and thus provided the shortest position update rate for the swarm. Fortunately, a new generation of the nanomodems (v3) features binary-phased-shift-keyed signals permitting overlapping ping receptions and providing a 10-fold increase in data rate, shorter pings, and improved error handing. Underwater GPS for an AUV has already been demonstrated (Neasham et al., 2021) and upgrade of the μFloats with v3 modems is currently underway.

6.2.1 Operations

μFloat operations proved straightforward and inexpensive. The sole vessel requirement was sufficient deck space to fit equipment and minimal personnel (captain and up to two crew members). Both μFloats and SLBs are lightweight and robust, permitting rapid deployment by a single crew member, though a second person was helpful for programming and spotting floats. Float recovery was sometimes challenging due to the small form factor. The radio and cellular relay of GPS locations proved essential to guide recovery vessels within visual distance, after which retrieval with a boat hook was simple. Glare, wave action, and fog complicated float sighting and recovery. For the Agate Pass test, the interval between recovery and redeployment ranged from 40-80 minutes and could be reduced further with operational practice or multiple recovery vessels.

Endurance of the μFloats is constrained by both the hotel load and the buoyancy engine. While floats for open ocean applications prioritize energy efficiency for longevity, the μFloat system was designed for short-term deployments (< 1 day) and prioritized cost-effectiveness and adaptability over energy efficiency. The hotel load is approximately 4 W and average buoyancy engine loads range between 3 and 4 W, resulting in a practical deployment endurance of about 12 hours. Greater endurance could be achieved by redesigning the electronics suite around a lower power microcontroller, reducing buoyancy engine actuation time, reducing float compressibility, and/or improving drivetrain efficiency.

6.3 Comparison to Other Floats

Through these benchmarking tests, we have demonstrated several advantages of the μFloat relative to existing coastal floats. The most notable of these is cost: at \$2.4k per float and \$3k per surface buoy, a swarm of 20 floats and 5 localization buoys costs ∼\$65k. The M-AUEs are comparable at \$6k per float (Jules Jaffe, pers. comm.) but their smaller form factor reduces buoyancy actuation. The second advantage is the μFloat's comparatively large buoyancy engine (9% actuation), which provides capacity for external sensors even in areas with sharp density gradients. A recently developed high-capacity float (Gene Massion, pers. comm.) is similar at 8% actuation and equipped with a suite of coastal oceanography instruments, but is significantly larger and more expensive. The commercially produced ALAMO float (4.2% actuation) can similarly traverse strong density gradients, but are an order of magnitude more expensive. The third advantage of the μFloat system is the nanomodem-based acoustic localization, which can provide position accuracy approaching that of GPS, as well as the ability to send commands and data between floats and the surface. While the M-AUE localization provides similar accuracy ($\pm$ 1.2 m) and longer range (<5 km), the system is restricted to one-directional localization (Jaffe et al., 2017) and cannot be used for general-purpose swarm coordination. Roman et al. utilizes ultra-short baseline localization that has lower accuracy ($\pm$ 15 m) and shorter range (250-1000 m), but supports higher bandwidth communications (14 kbit/s). Casagrande et al. (2019) recently investigated enhancements to these floats via terrain-based particle filter with visual odometry to improve positioning accuracy. The RAFOS localization system (Rossby et al., 1986) used with Argo and MLF floats provides basin-scale tracking (1400 km range, 1 km resolution) and is thus ill-suited for coastal-scale research. As such, the nanomodem array provides an appropriate balance of range, accuracy, flexibility, and cost for distributed sensor platforms in coastal environments. Lastly, the μFloat depth-holding accuracy ($<$ 10 cm in quiescent water and $<$ 50 cm in tidal flows) is matched only by Roman's hybrid propulsion approach (Snyder et al., 2018), albeit with slower dynamics.

The μFloat system does have several limitations. First, relative to other floats, the standard sensor suite (pressure, temperature, and IMU) is minimal. At a similar cost, the M-AUE includes a satellite modem for data transfer and recovery in regions without cellular networks, as well as a hydrophone for acoustic monitoring, though motor noise causes significant contamination when changing or holding depth ((Jaffe et al., 2017), Jules Jaffe, pers. comm.). The larger, more expensive floats (ALAMO, D'Asaro, Roman) have hosted a variety of additional sensors (e.g., salinity, pH, dissolved oxygen, acoustic Doppler velocimeters, and optical cameras). The μFloat's expansion capacity partially mitigates its sparse standard suite. As many sensors of interest (e.g., dissolved oxygen, pH) are more expensive than the μFloat itself, cost will primarily scale with the number of auxiliary sensors, and can be adjusted to the needs and budget of the end user. The second primary limitation is endurance, with the μFloats constrained to short duration ($<$ 1 day) deployments. The M-AUEs and Roman floats have similar endurance, but the ALAMO and D'Asaro floats are better suited for studying long-duration phenomena. Third, only depth control has been robustly demonstrated for the μFloat. Profiling (the primary Argo mode), isopycnal, and 3D Lagrangian control (implemented by D'Asaro) are also desirable. Additional control modes

include bottom-tracking, as implemented on the Roman float for visual surveys of biological communities (Roman et al., 2011; Snyder et al., 2018), and intermittent bottom-stationing, which was first demonstrated by Langebrake et al. (2002) with an Argo-style float. Finally, true Lagrangian behavior is optimized by reducing float size, and in this respect, the M-AUEs are superior.

6.4 Science Applications

While single drifting sensor packages provide considerable data of scientific interest, the μFloat system was developed specifically for swarm sensing. In the Agate Pass test, we demonstrated three-dimensional mapping of tidal currents relevant to coastal oceanography in general and to tidal energy resource extraction in particular (Blunden and Bahaj, 2007; Polagye and Thomson, 2013). Tidal energy sites are typically narrow ($<$ 10 km across) and shallow ($<$ 100 m deep) (Haas et al., 2011), with fast currents ($>$ 1.5 m/s) and strong gradients in both horizontal and vertical directions that make navigation with propeller-driven AUVs impractical. The μFloats proved to be an excellent platform for these environments, reaching target depths in an operationally practical time frame, and maintaining target depth within 1 m in minimally- or non-stratified water. When conditions support robust connectivity, the localization system provides along-track resolution of 1-10 m, depending on acoustic ping rate and local water speed. This matches the horizontal spatial resolution of vessel-mounted acoustic Doppler current profilers (5-10 m horizontal).

The μFloat system is also well suited to observing tidal plumes, fronts, and tidal bores. These systems have spatial extents on the order of 50 m to 5 km wide (Horner-Devine et al., 2015), with dynamics evolving on tidal time scales (0.25 to 12 hours), matching the sensing scale and endurance of the swarm. Density gradients in these regions can range from mild in well-mixed regions to nearly step-changes between fresh and salt water across tidal bores – extreme conditions unmanageable for previous floats but accommodated by the μFloat's buoyancy engine. For example, a swarm of μFloats instrumented with salinity sensors could volumetrically map salinity to improve salt flux estimates (MacDonald et al., 2007; McCabe et al., 2008).

Hydrophone-equipped floats could be useful for studying underwater soundscapes, a critical parameter for the health of many ecosystems (Duarte et al., 2021). While traditional acoustic surveys use vertical or horizontal arrays of hydrophones (Wilson et al., 2013; Macaulay et al., 2017), the μFloats would allow more flexible array configurations. Further, the Lagrangian nature of the float should reduce flow-noise across the hydrophone element (Bassett et al., 2014; Gobat and Grosenbaugh, 1997; Lighthill, 1954), improving fidelity of low-frequency noise measurements, though this will require modifications to the μFloat design to minimize self-noise from motor actuation.

Lastly, the μFloats are a compelling platform for preliminary evaluation of environmentally-aided navigation techniques (Langebrake et al., 2002; Jouffroy et al., 2011; Huynh et al., 2014; Smith and Huynh, 2014) in which the float selects target depths based on hydrodynamic models of the local currents to perform navigation tasks (e.g., station-keep, move between

waypoints). Such a technique could enable float persistence in an energetic area of interest. By utilizing the bidirectional nanomodem capabilities, μFloats could share environmental information across the swarm, enabling real-time coordination of float activity and adaptive sampling. While an area of active research for more mobile AUVs, such adaptive sampling has not yet been demonstrated for buoyancy-actuated float swarms. With improvements in system efficiency and co-deployment with other autonomous platforms, such as surface vehicles (Liu et al., 2016; Kimball et al., 2014) for robotic swarm management (e.g., recovery and redeployment), the μFloat could become an integral part of coastal autonomous sampling networks (Curtin et al., 1993; Curtin and Bellingham, 2009).

7 Conclusion

Understanding the health and dynamics of our coastal waterways is of vital importance. Observational platforms, both remote and *in situ*, are critical to this endeavour. This research expands the suite of tools available to scientists studying coastal waters and their phenomena with the introduction of the μFloat. The μFloat is an inexpensive ($2.4k) float with a high-capacity buoyancy engine that enables float swarm sensing in coastal environments. Fundamental performance characteristics have been detailed: the buoyancy engine provides depth control within $\pm$ 0.5 m, automatic ballasting from fresh to salt water, and accommodation of external sensors; consistent underwater acoustic localization was demonstrated with median position error of 5 m; and the three-dimensional hydrodynamic mapping capability of a swarm of twenty floats was demonstrated in a tidal channel with water speeds of 2 m/s. This work lays a foundation for the continued use of float swarms toward exploring the dynamics, physical properties, and soundscapes of our coastal waters.

Acknowledgements

The authors would like to acknowledge the following individuals who worked on μFloat design and manufacturing: Paul Gibbs, Kevin Zack, Justin Burnett, Zachary Tully, Andrew Witt, Jack Ryan, Kira Smith, Joshua Jaworski Castillo, and Chris Fisher.

For captaining vessels during testing, thanks to Alex de Klerk, Capt. Andy Reay-Ellers, and Chris Archer, as well as Paul Gibbs for an evening μFloat rescue mission. Thanks to Ariana Mendible for assistance with the Lake Washington field test. A special thanks to Adam Hill, Olivia Rogers, James Lindsay, and Alex Reid for their creation of the proto-μFloat during their capstone design project. Lessons learned then contributed directly to our current success. And final thanks are owed to Zoltan Szuts for a critical review and input on manuscript structure.

Funding: This material is based upon work supported by the National Science Foundation Graduate Research Fellowship under Grant No. DGE-1762114. Construction of the swarm was supported by ONR DURIP N00014-17-1-2336. Ongoing work is supported by the U.S. Department of Defense Naval Facilities Engineering Command under N0002410D6318

/ N0002418F8702.

References

Alford, M. H., Gregg, M. C., and D'Asaro, E. A. (2005). Mixing, 3d mapping, and lagrangian evolution of a thermohaline intrusion. *Journal of physical oceanography*, 35(9):1689–1711.

Arkema, K. K., Verutes, G. M., Wood, S. A., Clarke-Samuels, C., Rosado, S., Canto, M., Rosenthal, A., Ruckelshaus, M., Guannel, G., Toft, J., et al. (2015). Embedding ecosystem services in coastal planning leads to better outcomes for people and nature. *Proceedings of the National Academy of Sciences*, 112(24):7390–7395.

Bassett, C., Thomson, J., Dahl, P. H., and Polagye, B. (2014). Flow-noise and turbulence in two tidal channels. *The Journal of the Acoustical Society of America*, 135(4):1764–1774.

Blunden, L. and Bahaj, A. (2007). Tidal energy resource assessment for tidal stream generators. *Proceedings of the Institution of Mechanical Engineers, Part A: Journal of Power and Energy*, 221(2):137–146.

Bowden, K. F. (1983). *Physical oceanography of coastal waters*. Ellis Horwood Series on Marine Science.

Caron, F., Duflos, E., Pomorski, D., and Vanheeghe, P. (2006). Gps/imu data fusion using multisensor kalman filtering: introduction of contextual aspects. *Information fusion*, 7(2):221–230.

Casagrande, D., Krasnosky, K., and Roman, C. (2019). Localization of a drifting underwater vehicle using a terrain-based particle filter. In *OCEANS 2019 MTS/IEEE SEATTLE*, pages 1–8. IEEE.

Curtin, T. B. and Bellingham, J. G. (2009). Progress toward autonomous ocean sampling networks. *Deep Sea Research Part II: Topical Studies in Oceanography*, 56(3-5):62–67.

Curtin, T. B., Bellingham, J. G., Catipovic, J., and Webb, D. (1993). Autonomous oceanographic sampling networks. *Oceanography*, 6(3):86–94.

D'Asaro, E. (2015). Surface Wave Measurements from Subsurface Floats. *Journal of Atmospheric and Oceanic Technology*, 32(4):816–827.

D'Asaro, E. A. (2003). Performance of autonomous Lagrangian floats. *Journal of Atmospheric and Oceanic Technology*, 20(6):896–911.

D'Asaro, E. A. (2004). Lagrangian trajectories on the oregon shelf during upwelling. *Continental shelf research*, 24(13-14):1421–1436.

D'Asaro, E. A. (2014). Turbulence in the upper-ocean mixed layer. *Annual review of marine science*, 6:101–115.

D'Asaro, E. A., Farmer, D. M., Osse, J. T., and Dairiki, G. T. (1996). A Lagrangian Float. *Journal of Atmospheric and Oceanic Technology*, 13(6):1230–1246.

D'Asaro, E. A., Winters, K. B., and Lien, R.-C. (2002). Lagrangian analysis of a convective mixed layer. *Journal of Geophysical Research*, 107(C5).

Duarte, C. M., Chapuis, L., Collin, S. P., Costa, D. P., Devassy, R. P., Eguiluz, V. M., Erbe, C., Gordon, T. A. C., Halpern, B. S., Harding, H. R., Havlik, M. N., Meekan, M., Merchant, N. D., Miksis-Olds, J. L., Parsons, M., Predragovic, M., Radford, A. N., Radford, C. A., Simpson, S. D., Slabbekoorn, H., Staaterman, E., Van Opzeeland, I. C., Winderen, J., Zhang, X., and Juanes, F. (2021). The soundscape of the anthropocene ocean. *Science*, 371(6529).

D'Asaro, E. (2017). Oceanographic floats: principles of operation. *Observing the oceans in real time*, pages 77–98.

D'Asaro, E. A. and Dairiki, G. T. (1997). Turbulence intensity measurements in a wind-driven mixed layer. *Journal of physical oceanography*, 27(9):2009–2022.

D'Asaro, E. A. and Lien, R.-C. (2000). Lagrangian measurements of waves and turbulence in stratified flows. *Journal of physical oceanography*, 30(3):641–655.

Fenucci, D., Munafo, A., Phillips, A. B., Neasham, J., Gold, N., Sitbon, J., Vincent, I., and Sloane, T. (2018). Development of smart networks for navigation in dynamic underwater environments. In *2018 IEEE/OES Autonomous Underwater Vehicle Workshop (AUV)*, pages 1–6. IEEE.

Fringer, O. B., Dawson, C. N., He, R., Ralston, D. K., and Zhang, Y. J. (2019). The future of coastal and estuarine modeling: Findings from a workshop. *Ocean Modelling*, 143:101458.

Gobat, J. I. and Grosenbaugh, M. A. (1997). Modeling the mechanical and flow-induced noise on the surface suspended acoustic receiver. In *Oceans' 97. MTS/IEEE Conference Proceedings*, volume 2, pages 748–754. IEEE.

Gould, W. J. (2005). From swallow floats to argo—the development of neutrally buoyant floats. *Deep Sea Research Part II: Topical Studies in Oceanography*, 52(3-4):529–543.

Haas, K. A., Fritz, H. M., French, S. P., Smith, B. T., and Neary, V. (2011). Assessment of energy production potential from tidal streams in the united states. Technical report, Georgia Tech Research Corporation, Atlanta, GA (United States).

Harrison, T. (2021). *Buoyancy Controlled Float Swarms for Distributed Sensing in Coastal Waterways*. PhD thesis, University of Washington.

Horner-Devine, A. R., Hetland, R. D., and Macdonald, D. G. (2015). Mixing and Transport in Coastal River Plumes. *Annual Review of Fluid Mechanics*.

Huynh, V. T., Dunbabin, M., and Smith, R. N. (2014). Convergence-Guaranteed Time-Varying RRT Path Planning for Profiling Floats in 4-Dimensional Flow. In *Proceedings of the Australiasian Conference on Robotics and Automation*.

Jackson, D. R., Odom, R. I., Boyd, M. L., and Ivakin, A. N. (2010). A geoacoustic bottom interaction model (gabim). *IEEE Journal of Oceanic Engineering*, 35(3):603–617.

Jaffe, J. S., Franks, P. J. S., Roberts, P. L. D., Mirza, D., Schurgers, C., Kastner, R., and Boch, A. (2017). A swarm of autonomous miniature underwater robot drifters for exploring submesoscale ocean dynamics. *Nature Communications*, 8:1–8.

Jayne, S. R. and Bogue, N. M. (2017). Air-deployable profiling floats. *Oceanography*, 30(2):29–31.

Jayne, S. R., Roemmich, D., Zilberman, N., Riser, S. C., Johnson, K. S., Johnson, G. C., and Piotrowicz, S. R. (2017). The argo program: Present and future. *Oceanography*, 30(2):18–28.

Jouffroy, J., Zhou, Q., and Zielinski, O. (2011). Towards selective tidal-stream transport for lagrangian profilers. *Oceans 2011*, pages 1–6.

Kimball, P., Bailey, J., Das, S., Geyer, R., Harrison, T., Kunz, C., Manganini, K., Mankoff, K., Samuelson, K., Sayre-McCord, T., et al. (2014). The whoi jetyak: An autonomous surface vehicle for oceanographic research in shallow or dangerous waters. In *2014 IEEE/OES Autonomous Underwater Vehicles (AUV)*, pages 1–7. IEEE.

Langebrake, L. C., Lembke, C. E., Weisberg, R. H., Byrne, R. H., Russell, D. R., Tilbury, G., and Carr, R. (2002). Design and initial results of a bottom stationing ocean profiler. *OCEANS 2002*.

Lien, R.-C., D'Asaro, E. a., and Dairiki, G. T. (1998). Lagrangian frequency spectra of vertical velocity and vorticity in high-Reynolds-number oceanic turbulence. *Journal of Fluid Mechanics*, 362:177–198.

Lien, R.-C., D'Asaro, E. a., and McPhaden, M. J. (2002). Internal Waves and Turbulence in the Upper Central Equatorial Pacific: Lagrangian and Eulerian Observations. *Journal of Physical Oceanography*, 32(9):2619–2639.

Lighthill, M. J. (1954). On sound generated aerodynamically ii. turbulence as a source of sound. *Proceedings of the Royal Society of London. Series A. Mathematical and Physical Sciences*, 222(1148):1–32.

Liu, Y., Kerkering, H., and Weisberg, R. H. (2015). Chapter 1 - introduction to coastal ocean observing systems. In Liu, Y., Kerkering, H., and Weisberg, R. H., editors, *Coastal Ocean Observing Systems*, pages 1–10. Academic Press, Boston.

Liu, Z., Zhang, Y., Yu, X., and Yuan, C. (2016). Unmanned surface vehicles: An overview of developments and challenges. *Annual Reviews in Control*, 41:71–93.

Macaulay, J., Gordon, J., Gillespie, D., Malinka, C., Northridge, S., Macaulay, J., Gordon, J., and Gillespie, D. (2017). Passive acoustic methods for fine-scale tracking of harbour porpoises in tidal rapids. *The Journal of the Acoustical Society of America*, 1120.

MacDonald, D. G., Goodman, L., and Hetland, R. D. (2007). Turbulent dissipation in a near-field river plume: A comparison of control volume and microstructure observations with a numerical model. *Journal of Geophysical Research: Oceans*, 112(C7).

McCabe, R. M., Hickey, B. M., and MacCready, P. (2008). Observational estimates of entrainment and vertical salt flux in the interior of a spreading river plume. *Journal of Geophysical Research: Oceans*, 113(C8).

McGilvray, B. and Roman, C. (2010). Control system performance and efficiency for a mid-depth lagrangian profiling float. *IEEE OCEANS 2010 - SYDNEY*.

Neasham, J. (2016). Usmart project website. `https://research.ncl.ac.uk/usmart/`. Accessed May 2021.

Neasham, J., Chawla, A., Sherlock, B., and Loncar, I. (2021). A multi-user underwater acoustic positioning system – experiments using asvs and miniature acoustic transceivers. In *2021 OCEANS San Diego*, pages 1–5. IEEE.

Norrdine, A. (2012). An algebraic solution to the multilateration problem. In *2012 International Conference on Indoor Positioning and Indoor Navigation*.

Polagye, B. and Thomson, J. (2013). Tidal energy resource characterization: methodology and field study in Admiralty Inlet, Puget Sound, WA (USA). *Proceedings of the Institution of Mechanical Engineers, Part A: Journal of Power and Energy*, 227(3):352–367.

Raggi, E. (2019). *Localization of a Drifting Underwater Vehicle Using a Terrain-Based Particle Filter*. PhD thesis, University of Rhode Island. Copyright - Database copyright ProQuest LLC; ProQuest does not claim copyright in the individual underlying works; Last updated - 2020-11-03.

Riser, S. C., Freeland, H. J., Roemmich, D., Wijffels, S., Troisi, A., Belbeoch, M., Gilbert, D., Xu, J., Pouliquen, S., Thresher, A., Le Traon, P.-Y., Maze, G., Klein, B., Ravichandran, M., Grant, F., Poulain, P.-M., Suga, T., Lim, B., Sterl, A., Sutton, P., Mork, K.-A., Velez-Belchi, P. J., Ansorge, I., King, B., Turton, J., Baringer, M., and Jayne, S. R. (2016). Fifteen years of ocean observations with the global Argo array. *Nature Clim. Change*, 6(2):145–153.

Roark, R. J., Young, W. C., and Plunkett, R. (1976). Formulas for stress and strain.

Roman, C., Inglis, G., and McGilvray, B. (2011). Lagrangian floats as sea floor imaging platforms. *Continental Shelf Research*, 31(15):1592–1598.

Rossby, T. (2007). Evolution of lagrangian methods in oceanography. *Lagrangian Analysis and Prediction of Coastal and Ocean Dynamics*, pages 1–38.

Rossby, T., Dorson, D., and Fontaine, J. (1986). The rafos system. *Journal of atmospheric and oceanic technology*, 3(4):672–679.

Schulze Chretien, L. M. and Speer, K. (2018). Observing plumes and overturning cells with a new coastal bottom drifter. *Journal of Atmospheric and Oceanic Technology*, 35(8):1675–1686.

Schwithal, A. and Roman, C. (2009). Development of a new Lagrangian float for studying coastal marine ecosystems. *OCEANS 2009 - Europe*, pages 1–6.

Shcherbina, A. Y., D'Asaro, E. A., and Nylund, S. (2018). Observing finescale oceanic velocity structure with an autonomous nortek acoustic doppler current profiler. *Journal of Atmospheric and Oceanic Technology*, 35(2):411–427.

Smith, J. and Abel, J. (1987). Closed-form least-squares source location estimation from range-difference measurements. *IEEE Transactions on Acoustics, Speech, and Signal Processing*, 35(12):1661–1669.

Smith, R. N. and Huynh, V. T. (2014). Controlling buoyancy-driven profiling floats for applications in ocean observation. *IEEE Journal of Oceanic Engineering*, 39(3):571–586.

Snyder, W., Roman, C., and Licht, S. (2018). Hybrid actuation with complementary allocation for depth control of a lagrangian sea-floor imaging platform. *Journal of Field Robotics*, 35(3):330–344.

Steffen, E. L. and D'Asaro, E. A. (2002). Deep convection in the labrador sea as observed by lagrangian floats. *Journal of Physical Oceanography*, 32(2):475–492.

Thomson, J., Moulton, M., de Klerk, A., Talbert, J., Guerra, M., Kastner, S., Smith, M., Schwendeman, M., Zippel, S., and Nylund, S. (2019). A new version of the swift platform for waves, currents, and turbulence in the ocean surface layer. In *IEEE/OES Workshop on Currents, Waves, and Turbulence Measurements*.

Wilkin, J., Rosenfeld, L., Allen, A., Baltes, R., Baptista, A., He, R., Hogan, P., Kurapov, A., Mehra, A., Quintrell, J., et al. (2017). Advancing coastal ocean modelling, analysis, and prediction for the us integrated ocean observing system. *Journal of Operational Oceanography*, 10(2):115–126.

Wilson, B., Benjamins, S., and Elliott, J. (2013). Using drifting passive echolocation loggers to study harbour porpoises in tidal-stream habitats. *Endangered Species Research*, 22(2):125–143.

Wong, A. P., Wijffels, S. E., Riser, S. C., Pouliquen, S., Hosoda, S., Roemmich, D., Gilson, J., Johnson, G. C., Martini, K., Murphy, D. J., et al. (2020). Argo data 1999–2019: Two million temperature-salinity profiles and subsurface velocity observations from a global array of profiling floats. *Frontiers in Marine Science*.